























GRB 230204B: GIT Discovery of a Fast Fading Afterglow Associated with an Energetic GRB from a Massive-Star Progenitor

VISHWAJEET SWAIN ¹, VARUN BHALERAO ¹, HARSH KUMAR ^{1,2}, MEHUL GOYAL ¹, ANKUR GHOSH ³,
UTKARSH PATHAK ¹, POONAM CHANDRA ⁴, TOMÁS AHUMADA ⁵, G. C. ANUPAMA ⁶, S. BALA ⁷,
SUDHANSHU BARWAY ⁶, JOSHUA S. BLOOM ⁸, DIMPLE ⁹, VIRAJ KARAMBELKAR ⁵, MANSI KASLIWAL ⁵,
KUNTAL MISRA ¹⁰, JOSIAH PURDUM ¹¹, DIVITA SARAOGI ¹, JESPER SOLLERMAN ¹², ASWIN SURESH ^{13,14},
STÉFAN VAN DER WALT ¹⁵ AND GAURAV WARATKAR ^{5,1}

¹Department of Physics, Indian Institute of Technology Bombay, Powai, 400076, India

²Center for Astrophysics | Harvard & Smithsonian, 60 Garden Street, Cambridge, MA 02138-1516, USA

³Centre for Astro-Particle Physics (CAPP) and Department of Physics, University of Johannesburg, PO Box 524, Auckland Park 2006, South Africa

⁴National Radio Astronomy Observatory, Charlottesville VA 22903, USA

⁵Cahill Center for Astrophysics, California Institute of Technology, MC 249-17, 1216 E California Boulevard, Pasadena, CA, 91125, USA

⁶Indian Institute of Astrophysics, II Block Koramangala, Bengaluru 560034, India

⁷Science and Technology Institute, Universities Space Research Association, Huntsville, AL 35805, USA

⁸Department of Astronomy, University of California, Berkeley, CA 94720-3411, USA

⁹School of Physics and Astronomy, University of Birmingham, Edgbaston, Birmingham, B15 2TT, UK, Institute for Gravitational Wave Astronomy, University of Birmingham, Birmingham, B15 2TT, UK.

¹⁰Aryabhatta Research Institute of Observational Sciences, Manora Peak, Nainital 263129, India

¹¹Caltech Optical Observatories, California Institute of Technology, Pasadena, CA 91125

¹²The Oskar Klein Centre, Department of Astronomy, Stockholm University, AlbaNova, SE-10691 Stockholm, Sweden

¹³Department of Physics and Astronomy, Northwestern University, Evanston, IL 60208, USA

¹⁴Center for Interdisciplinary Exploration and Research in Astronomy, Northwestern University, 1800 Sherman Avenue, Evanston, IL 60201, USA

¹⁵Berkeley Institute for Data Science, University of California Berkeley, Berkeley, CA 94720, USA

ABSTRACT

We present a comprehensive multi-wavelength study of a bright gamma-ray burst GRB 230204B, analyzing both prompt and afterglow emissions. This GRB is highly energetic, with an isotropic equivalent energy emission $E_{\text{iso}} \sim 2.2 \times 10^{54}$ erg, released during the prompt emission. The GROWTH-India Telescope discovered a bright afterglow ($m_r = 15.55$) that faded rapidly ($\propto t^{-1.82}$). The prompt emission shows strong thermal photospheric emission, along with a non-thermal high-energy component. We explore the evolution of these components and find them to be consistent with theoretical expectations. Afterglow modeling reveals an energetic jet $E_{\text{tot}} \gtrsim 10^{52}$ erg expanding into a wind-type medium viewed nearly on-axis, suggesting a massive star progenitor with strong winds. We also explore correlations between the prompt emission and afterglow that may help to understand the complete picture of GRB progenitors.

Keywords: Gamma-ray bursts (629) Burst astrophysics (187) Relativistic jets (1390) Wolf-Rayet stars (1806)

1. INTRODUCTION

Long Gamma Ray Bursts (LGRBs) are highly energetic explosions with strong relativistic jets, associated with the death of a massive stars (A. I. MacFadyen & S. E. Woosley 1999; T. Piran 2004; S. Woosley & J. Bloom 2006). Observations indicate that the collimation-corrected gamma-ray energy re-

lease from GRBs is typically on the order of 10^{51} erg, with isotropic-equivalent energy (E_{iso}) spanning a broad range from 10^{48} to 10^{55} erg (T. Piran 2004; P. Kumar & B. Zhang 2015). GRBs with $E_{\text{iso}} > 10^{54}$ erg are commonly classified as energetic GRBs (L. Lan et al. 2023). The collapse of rapidly rotating Wolf-Rayet stars is considered a plausible progenitor channel for these highly energetic events (S. Woosley & J. Bloom 2006).

The prompt emission of GRBs is usually non-thermal in nature and the time-integrated spectrum is typically modeled by the empirical Band function (D. Band et al. 1993; F. Massaro et al. 2010; F. J. Virgili et al. 2012). However, this model lacks a direct physical interpretation. In time-resolved spectroscopy using smaller time bins, the spectra can sometimes still be fit with a Band function, but in other cases, they can be fit with physically motivated models such as blackbody (BB), cut-off power-law (CPL), or combinations like power-law plus blackbody (PL+BB), Band+BB, etc. (B.-B. Zhang et al. 2011; F. Ryde et al. 2010; M. G. Bernardini et al. 2017).

The standard fireball model predicts the presence of photospheric emission, along with non-thermal emission from internal shocks (G. Cavallo & M. J. Rees 1978; M. J. Rees & P. Meszaros 1994). The spectral shape of photospheric emission is typically a blackbody, but under certain physical conditions, it can broaden and resemble the Band function (B.-B. Zhang et al. 2011; S. Iyyani et al. 2013). Some GRBs, like GRB 110721A (S. Iyyani et al. 2013), are well described by BB+Band models, where the Band component is interpreted as non-thermal emission.

The spectral properties can thus be used to interpret the nature of the emission components. For instance, GRB 090902B (F. Ryde et al. 2010), with $E_{\text{iso}} \sim 10^{52}$ erg, is well fit by the PL+BB model, indicating signatures of photospheric emission. In such models, the PL component is attributed to non-thermal emission, while the BB component originates from the photosphere of the expanding relativistic jet (F. Ryde et al. 2010). The signature of the blackbody component in the GRB prompt spectra could indicate that the jet is matter dominated and is not highly magnetized (P. Veres et al. 2012; S. Iyyani et al. 2013). On the other hand, the energetic GRB 080916C displays a featureless spectrum well fit by a Band function alone and shows characteristics consistent with a Poynting flux-dominated jet with a high magnetic field (B.-B. Zhang et al. 2011).

Overall, the composition of GRB jets — whether they are matter-dominated, Poynting flux-dominated, or exhibit a hybrid nature — remains an open question. The role of magnetization near or above the photosphere is also still not fully understood.

After the release of gamma-ray energy during the prompt emission phase, the fireball ejecta, moving at relativistic speeds, interact with the circum-burst medium and produce multi-wavelength afterglow emission (R. Sari et al. 1998; Z.-Y. Li & R. A. Chevalier 2003; A. Pe’er & F. Ryde 2024). More than 500 GRB afterglows have been detected and studied since the first X-

ray and optical discovery in Feb 1997 (M. G. Dainotti et al. 2024). Over the past few years, wide-field time-domain surveys have significantly advanced our ability to discover and characterize optical counterparts of high-energy transients. In particular, the Zwicky Transient Facility (ZTF; E. C. Bellm et al. 2019; M. J. Graham et al. 2019; R. Dekany et al. 2020; F. J. Masci et al. 2019) has played a leading role in the systematic discovery and follow-up of GRB afterglows and fast X-ray transients, owing to its high cadence and wide sky coverage. LGRBs are usually associated with massive star progenitors, whose environments are expected to be shaped by stellar winds released prior to the burst (R. A. Chevalier & Z.-Y. Li 2000). Although some GRBs are consistent with the expected wind-type environments, many others are better fitted by a uniform density medium (A. Panaitescu & P. Kumar 2001; Z.-Y. Li & R. A. Chevalier 2003; X.-G. Wang et al. 2015). Other works suggest that a uniform density region surrounding a massive star can result from a wind termination shock, which becomes possible if the mass-loss rate is reduced to $10^{-6} M_{\odot} \text{ yr}^{-1}$ due to the low metallicity of the progenitor star (R. A. M. J. Wijers & T. J. Galama 1999; Z.-Y. Li & R. A. Chevalier 2003).

For some sources, it is difficult to distinguish between an ISM and a wind environment using data available only a few days post-burst (Z.-Y. Li & R. A. Chevalier 2003; A. Panaitescu & P. Kumar 2001). A wind-type circum-burst medium is typically identified using radio data, where the light curve is expected to remain flat for days. Another possible signature of the wind-type medium is a steep decay in the optical light curve. However, this can also be caused by a highly collimated jet (R. Sari & T. Piran 1999; A. Panaitescu & P. Kumar 2001).

In this paper, we present the discovery of the optical afterglow of GRB 230204B (V. Swain et al. 2023) from the GROWTH-India Telescope (GIT; H. Kumar et al. 2022) along with a comprehensive multiwavelength analysis incorporating data from various facilities. Through coordinated efforts, we have obtained long-term follow-up observations across multiple wavelengths, enabling a detailed analysis of various physical aspects of GRB 230204B.

A parallel study of GRB 230204B conducted by R. Gupta et al. (2024) focused on the spectral modeling of the prompt emission and reported a hybrid jet composition, with evidence for the thermal component. From broadband modeling of the optical afterglow, they interpreted the event as a highly collimated jet propagating into a homogeneous circum-burst medium. They inferred a very low radiative efficiency of approximately

4% and emphasized the exceptionally luminous optical afterglow.

In contrast, our work focuses on a detailed investigation of the prompt-emission physics through extensive spectral modeling, including PL+BB diagnostics that allow direct constraints on the Lorentz factor, photospheric radius, and base radius of the outflow. We perform broadband afterglow modeling in a wind-type environment, motivated by both the early steep decay and late-time radio constraints. While we also find evidence for a collimated jet, we further interpret the bright and rapidly fading nature of this GRB, constrain its true energy budget, and infer its progenitor to be a massive Wolf–Rayet star. Finally, we place GRB 230204B in the broader context of the GRB population using empirical correlations spanning both prompt and afterglow properties.

Our paper is organized as follows. Section 2 describes the multi-wavelength observations obtained from various facilities, along with data reduction procedures, supplemented by publicly available data reported through Gamma-ray Coordinates Network (GCN) Circulars. Section 3 presents the prompt emission analysis using *Fermi* GBM data, including time-integrated and time-resolved spectral modeling with multiple emission models. In Section 4, we place GRB 230204B in the context of global empirical correlations and interpret the physical implications of the time-resolved spectral parameters. The afterglow light curves and spectral properties are analyzed in Section 5, followed by detailed modeling of the afterglow evolution in both interstellar medium (ISM) and wind-stratified environments in Section 6. Finally, we explore correlations between prompt and afterglow parameters in §7, and discuss factors contributing to the efficient energy release in energetic GRBs, the rapid decay observed in the afterglow of GRB 230204B, and implications for the progenitor system.

2. OBSERVATIONS

GRB 230204B was first detected by *MAXI-GSC* nova alert system at trigger time (T_0), 21:47:51 UT on Feb 4, 2023 (M. Serino et al. 2023). A bright source was located at the position of RA (J2000): 13h 10m 19s and Dec (J2000): $-21^{\circ}45'07''$, with an elliptical error region long and short radii of 0.12 deg and 0.1 deg at the statistical 90% confidence level. The X-ray flux averaged over the scan was 628 ± 49 mCrab (4.0–10.0 keV, 1- σ error). In addition, *AstroSat* CZTI (G. Waratkar et al. 2023), *Fermi* GBM (S. Poolakkil et al. 2023), *AGILE* (C. Casentini et al. 2023), *GRBAlpha* (M. Dafcikova et al. 2023) detected the burst in their energy ranges.

The GROWTH-India Telescope (GIT) was triggered as soon as the target became visible, ≈ 1.5 hours after *Fermi* GBM trigger time T_0 , to search for the optical counterpart. GIT located a new source at RA (J2000): 13h 10m 19s and Dec (J2000): $-21^{\circ}45'07''$, with an uncertainty of $0.67''$, shown in Figure 1. The source was found to be rapidly fading, and was confirmed to be the GRB afterglow. Using the initial large dataset obtained in the r -band, GIT reported its discovery of the optical afterglow and the rapid temporal decay of the source on the General Coordinates Network (V. Swain et al. 2023). As part of the GROWTH collaboration (M. M. Kasliwal et al. 2019), we triggered additional observations with several other telescopes (§2.2). We utilize the ZTF Fritz marshal to trigger the telescopes and store the photometric data (S. van der Walt et al. 2019; M. W. Coughlin et al. 2023). Unfortunately, due to poor weather conditions at some of the observatories, we obtained a limited dataset. Independent VLT/X-shooter observations captured the GRB afterglow spectrum and determined the redshift to be $z = 2.142$ (A. Saccardi et al. 2023). Other observations were independently acquired by several groups, ranging from pre-discovery images to late time observations (see for instance R. Gupta et al. 2024). We have utilized some publicly available data in our analysis (§2.2.5).

Throughout this work, we adopt the *Planck*2018 cosmology in *astropy* with $H_0 = 67.66$ km s $^{-1}$ Mpc $^{-1}$ and $\Omega_m = 0.30966$. For this redshift, the corresponding luminosity distance is $D_L = 5.34 \times 10^{28}$ cm (or 17.3 Gpc).

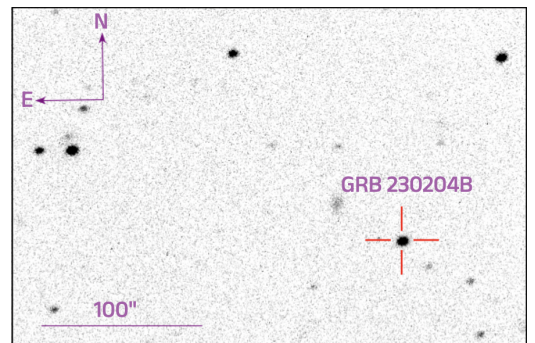


Figure 1. The optical afterglow of GRB 230204B was discovered by the GROWTH-India Telescope (GIT) in r' filter at UT 2023-02-04T23:22:37.6, as reported by V. Swain et al. (2023). The source was both bright and rapidly fading, consistent with the expected behavior of a GRB afterglow.

2.1. Prompt emission

The prompt emission of the bright GRB 230204B was observed by various space instruments. For the analysis

we mainly used the data from *Fermi*-GBM for both time integrated and time resolved analysis.

2.1.1. *Fermi*-GBM

Fermi GBM was triggered at time $T_0 = 21:47:51$ UT on Feb 04, 2023 (S. Poolakkil et al. 2023). Here, we report the results of an analysis of the *Fermi*-GBM prompt data. GBM has 12 NaI detectors (8 keV–1 MeV) and two BGO detectors (200 keV–40 MeV). We choose the detectors according to the brightness of the spectral counts and the angle of the detector’s boresight to the source location. The source was detected as bright in the NaI 8 detector, at 18° away from the source. For analysis, we used two NaI detectors, NaI 7 and NaI 8, and a single BGO detector, BGO 1. The angle from the *Fermi* LAT boresight at the GBM trigger time is 106° , thus LAT data are not included in the analysis (M. Ackermann et al. 2012). The duration of the GRB is $T_{90} = 216$ s in the energy range of 50–300 keV. The strongest peak occurred at $T_0 + 156$ s in the energy range of 10–1000 keV with a photon flux of 7.3 ± 0.4 ph s $^{-1}$ cm $^{-2}$ (S. Poolakkil et al. 2023).

2.1.2. *AstroSat* CZTI

The source was also seen by *AstroSat* Cadmium Zinc Telluride Imager (*AstroSat*-CZTI; V. Bhalerao et al. 2017), where both the CZT modules (20–200 keV) and the Veto detectors (100–500 keV) detected multiple peaks of the emission (G. Waratkar et al. 2021). The strongest peak in the CZT detectors occurred at $T_0 + 51.5$ s, whereas in the Veto detectors the strongest peak occurred at $T_0 + 50.8$ s. Our detailed re-analysis of the data shows that the peak count rate in the CZT was 548 ± 50 counts s $^{-1}$ above background, with a total of $23,613^{+1,157}_{-353}$ counts and a T_{90} duration of $221.9^{+4.2}_{-5.3}$ s, consistent with the *Fermi*-GBM T_{90} . In the Veto, the peak count rate was 1324^{+78}_{-86} counts s $^{-1}$ above background, with a total of $51,434^{+1332}_{-1566}$ counts and a T_{90} of 229^{+22}_{-28} s. A total of 3240 Compton events were associated with the burst; however, the detector was at a boresight angle of 75° , which is too large to perform polarization analysis (T. Chattopadhyay et al. 2022).

2.2. Multiband Afterglow

For broad-band afterglow analysis, we utilized the data from the observations by GROWTH-India Telescope (GIT), the Palomar 60-inch telescope (P60), Devasthal Optical Telescope (DOT), Giant Metrewave Radio Telescope (GMRT), Very Large Array (VLA) and other public data taken from GCN, are described below.

2.2.1. GIT

We used GIT located at the Indian Astronomical Observatory (IAO), Hanle-Ladakh, to acquire data of GRB 230204B optical afterglow (H. Kumar et al. 2022). GIT is a 0.7-meter, wide-field, fully robotic telescope specifically designed for the study of transient astrophysical events. The afterglow was observed in a Sloan r' filter starting at 1.57 h after the GRB detection at 2025-02-04T21:47:51 UT by *MAXI-GSC* (M. Serino et al. 2023). Data were downloaded and processed in real time by the GIT data reduction pipeline. Basic reduction, astrometry, and point-spread-function (PSF) photometry followed the procedure described in H. Kumar et al. (2022). The final magnitudes were calibrated against Pan-STARRS.

2.2.2. P60/SEDM

Once the afterglow was identified, we used the Rainbow Camera on the Spectral Energy Distribution Machine (SEDM; N. Blagorodnova et al. 2018; M. Rigault et al. 2019) mounted on the Palomar 60-inch telescope to acquire r - and i - band imaging in 300 s exposures, starting 10.88 hours after the burst. The SEDM images were processed with a python-based pipeline version of *Fpipe* (Fremling Automated Pipeline; C. Fremling et al. 2016), which includes photometric calibrations. Afterglow spectroscopy was attempted, but unfortunately, the weather conditions did not allow for good signal-to-noise observations.

2.2.3. Radio

We conducted multiple follow-up observations with the Giant Metrewave Radio Telescope (GMRT) and the Very Large Array (VLA) at different epochs following the initial trigger. The GMRT observations, carried out on Feb 22, 2023, obtained an upper limit in Band 5 (1000–1450 MHz). The VLA observations, beginning on Feb 15, 2023, and extending over several epochs, yielded multiple detections in the X band (8–12 GHz; central frequency 10 GHz) and upper limits in the S band (2–4 GHz). A summary of the measured fluxes and upper limits from all observing epochs is presented in the supplementary material at V. Swain et al. (2025)¹⁶.

2.2.4. Swift-XRT

Observations with *Swift*-XRT began approximately 80.6 ks after the trigger time. For the light curve analysis, we utilized the results publicly available from the

¹⁶ https://zenodo.org/records/17782846/files/Table_afterglow_obs.csv?download=1

UK Swift Science Data Centre (UKSSDC)¹⁷. In the afterglow analysis, we considered two data points of unabsorbed flux density at 10 keV, and ignored the very weak upper limit at the third epoch.

We reanalyzed the data of the first interval to obtain some spectral parameters. Since the optical light curve showed no evidence of flares or temporal breaks, we performed a time-integrated analysis over the interval from $T_0 + 80.6$ ks to 110.0 ks in the 0.3–10 keV energy band. The X-ray data were obtained from *Swift* observations as described by P. A. Evans et al. (2007). The total number of observed counts was 17, which is insufficient for spectral fitting due to the large number of free parameters. Therefore, we fixed the value of the intrinsic hydrogen column density to the mean value of $N_H = 2.2 \times 10^{21} \text{ cm}^{-2}$ as reported by P. A. Evans et al. (2007). With this assumption, we performed a likelihood-based spectral fit using *ThreeML*, yielding a photon index of 1.4 ± 0.4 . It corresponds to a spectral index of $\beta = 0.4 \pm 0.4$. The resulting flux is $2.3 \times 10^{-13} \text{ erg s}^{-1} \text{ cm}^{-2}$ in the 0.3–10 keV band. The results are consistent with the automated analysis provided by the UKSSDC.

2.2.5. Other Public Data

We used publicly available photometric detections from Asteroid Terrestrial-impact Last Alert System (ATLAS, S. J. Smartt et al. 2023), 3.6-meter DOT (A. K. Ror et al. 2023; R. Gupta et al. 2024), VLT/X-shooter (A. Saccardi et al. 2023) and Australia Telescope Compact Array (ATCA, A. Gulati et al. 2023) published through GCN. All the photometric data points are presented in the supplementary material at V. Swain et al. (2025).

3. PROMPT EMISSION: ANALYSIS

We retrieved the *Fermi*-GBM data TTE and CSPEC mode of GRB 230204B from the *Fermi* Science Support Center archives¹⁸ and processed it with *ThreeML* (G. Vianello et al. 2015). Throughout this work, we use the *Fermi* trigger time $T_0 = 2023-02-04T21:44:27.20$ as the reference time.

3.1. Time-integrated Analysis

To model the full burst spectrum, we selected data in the time range from $T_0 - 0.81$ s to $T_0 + 229.96$ s. First we extracted the background and light curves of the GBM data. Following standard practices in *ThreeML*, CSPEC mode data was used for background estimation

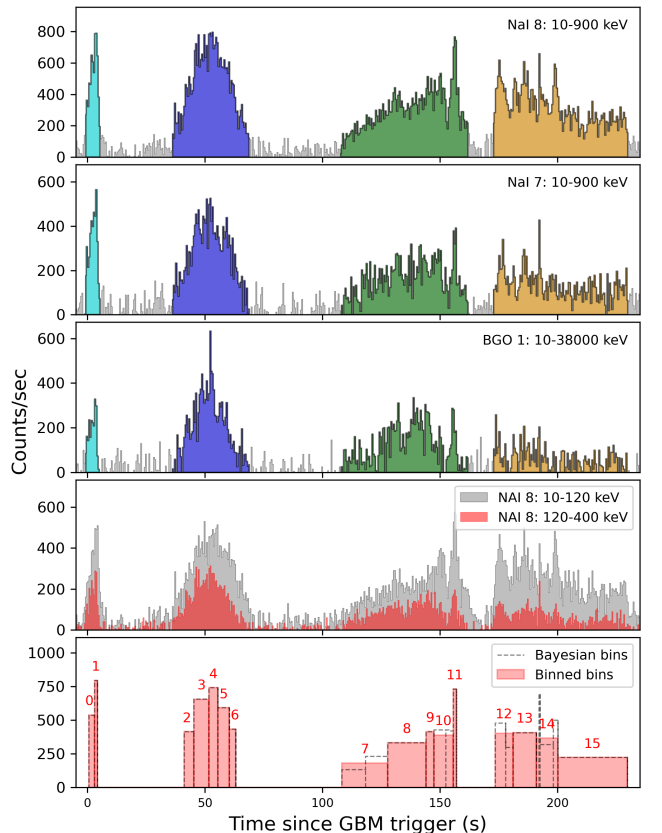


Figure 2. Multi-panel light curve analysis of GRB 230204B using *Fermi*-GBM detectors. Top panels: Background-subtracted light curves from NaI detectors 8 and 7 (10–900 keV), and BGO detector 1 (10–38,000 keV), color-coded by episode. Middle panel: Comparison of low-energy (10–120 keV) and mid-energy (120–400 keV) light curves from NaI 8, highlighting the spectral evolution during the burst. The structure reveals four distinct emission episodes, with significant variability in intensity and spectral hardness across them. Bottom panel: Bayesian blocks (dashed gray) and final binned intervals (shaded red) used for time-resolved spectral analysis, labeled with bin numbers. The binning ensures sufficient counts in high-energy channels (e.g., BGO 1) for reliable spectral fitting. Figure is plotted with packages – *GDT-Core* (A. Goldstein et al. 2023) and *ThreeML* (G. Vianello et al. 2015).

as they have wider temporal coverage, while event data were extracted from TTE mode data. Energy dependent background light curves were modeled with polynomial functions. We used the commonly used energy range from 250 keV to 38 MeV for BGO detectors and 10 keV – 900 keV for NaI detectors. The final background-subtracted light curves are shown in Figure 2.

We undertook spectral fitting using various models available in *ThreeML/astromodels* and utilized a Bayesian fitting method with the *multi-nest* sampler with 5000 live points. Of the commonly used models

¹⁷ https://www.swift.ac.uk/xrt_live_cat/00021535/

¹⁸ <https://fermi.gsfc.nasa.gov/ssc/data/access/>

for GRB spectra, we obtained reasonable fits for a Band spectrum, a cut-off power-law (CPL), and a combination of a power-law (PL) and a blackbody (BB) component (Table 1). To compare the fits from various models, we used both the Akaike Information Criterion (AIC) and the Bayesian Information Criterion (BIC). We found that the time-integrated spectrum is best modeled by the PL + BB model and also reasonably well fit by the Band and CPL models. The time-integrated spectrum gives the average temperature of the BB component $kT = 65.4 \pm 3.0$ keV with PL index of $\Gamma = -1.49 \pm 0.03$. We note that Band function values of the low-energy power-law slope $\alpha = -0.85^{+0.05}_{-0.03}$ and the peak energy $E_p = 560^{+48}_{-63}$ keV agree with the low energy spectral slope and cut-off energy for the CPL model. Adding a BB component to Band and CPL models did not significantly impact the quality of the fit, and BB parameters were poorly constrained — hence we exclude these from further discussion.

3.2. Episode-wise Analysis

The light curves of GRB 230204B display four distinct episodes which can be interpreted as the central engine switching on and off multiple times. The width of the first episode is narrow, and it increases for subsequent episodes. We analyzed each episode separately, using time spans listed in Table 1¹⁹ and shown in Figure 2. Data for each episode was extracted following the procedure discussed in Section 3.1, and fit with the same three spectral models. The results (Table 1) show that the two brighter episodes (second and third) are best fit with the Band function while the first and fourth are best fit with the PL + BB model. The Band function again gives a better fit than CPL, and the values of α and E_p from the two models are consistent with each other as in the case of the time-integrated analysis. The low energy spectral index α shows evolution from hard ($\alpha = -0.34 \pm 0.10$) to soft ($\alpha = -0.82 \pm 0.05$) spectra.

In particular for the first episode, the value $\alpha = -0.34 \pm 0.10$ is harder than the canonical value of $\alpha = -1$ for typical GRBs (B.-B. Zhang et al. 2011; S. Poolakkil et al. 2021). This hard spectrum hints the presence of photospheric emission (F. Ryde et al. 2010; B.-B. Zhang et al. 2011). Both BB temperature and peak energy E_p show a similar trend across the episodes. Episode 3 has the highest peak energy of $E_p = 796 \pm 87$ keV and BB temperature of $kT = 90.2 \pm 5.0$ keV, showing the hardest spectrum among all episodes.

Comparing the fluence in the observed energy range (10 keV to 38 MeV) in each episode, we find that the first episode contributes $\sim 6\%$ of the total energy output, the second contributes $\sim 33\%$, the third $\sim 36\%$, and the fourth $\sim 25\%$. For the first three episodes, the blackbody fraction is roughly 17-18%, but drops to $\sim 12\%$ in Episode 4. Such a decline is expected as the photosphere expands, cools, and becomes transparent, allowing non-thermal processes to dominate. The early episodes, therefore, appear consistent with a hot, weakly magnetized fireball in which photospheric emission is prominent.

3.3. Time-resolved Analysis

For the time-resolved analysis, we first take the brightest detector, NaI 8, and divide the light curve into Bayesian blocks using a false alarm probability threshold $P = 0.01$. The Bayesian blocks algorithm converts the time-series data into an optimal piecewise constant representation (J. D. Scargle et al. 2013), but does not guarantee a sufficiently high number of counts in each block. This was particularly an issue for the high-energy spectra from the detector BGO 1. To mitigate this issue, we grouped consecutive Bayesian blocks into bins until the statistical significance of the BGO 1 data was at least $5\text{-}\sigma$ for each bin. We ensured that we did not combine blocks from the four distinct episodes in the burst. The procedure gave us a total of 16 time bins as shown in Figure 2. We exclude the time intervals between episodes where the central engine was inactive. We also exclude the bins in the rising and decaying phases of each episode that lacked sufficient significance.

We undertook spectral analysis for each bin using the Band and PL + BB models. For both the models, the detailed fit values are available in the supplementary material at V. Swain et al. (2025)²⁰. We excluded the CPL model as it gives consistent results with the Band function, but had higher AIC and BIC values in the time-integrated and episode-wise analysis. The results of the fits showed that the PL + BB model provided a better fit than the Band model for most time bins. However, for bin-8 (duration ~ 16 s) in Episode 3 — corresponding to the highest peak energy and BB temperature — the Band model yielded a slightly better fit as compared to PL+BB model, with $\Delta\text{AIC} = 12$ and $\Delta\text{BIC} = 12$.

For the Band model, α ranges from the hard (-0.002) to soft (-0.97) spectrum with mean of -0.62 . The spectrum is the hardest in bin-1, indicating optical thick emission. The harder spectra (higher values of α in the

¹⁹ Episode boundaries were selected manually to coincide with the closest Bayesian block boundaries, which are discussed in Section 3.3.

²⁰ <https://zenodo.org/records/17782846>

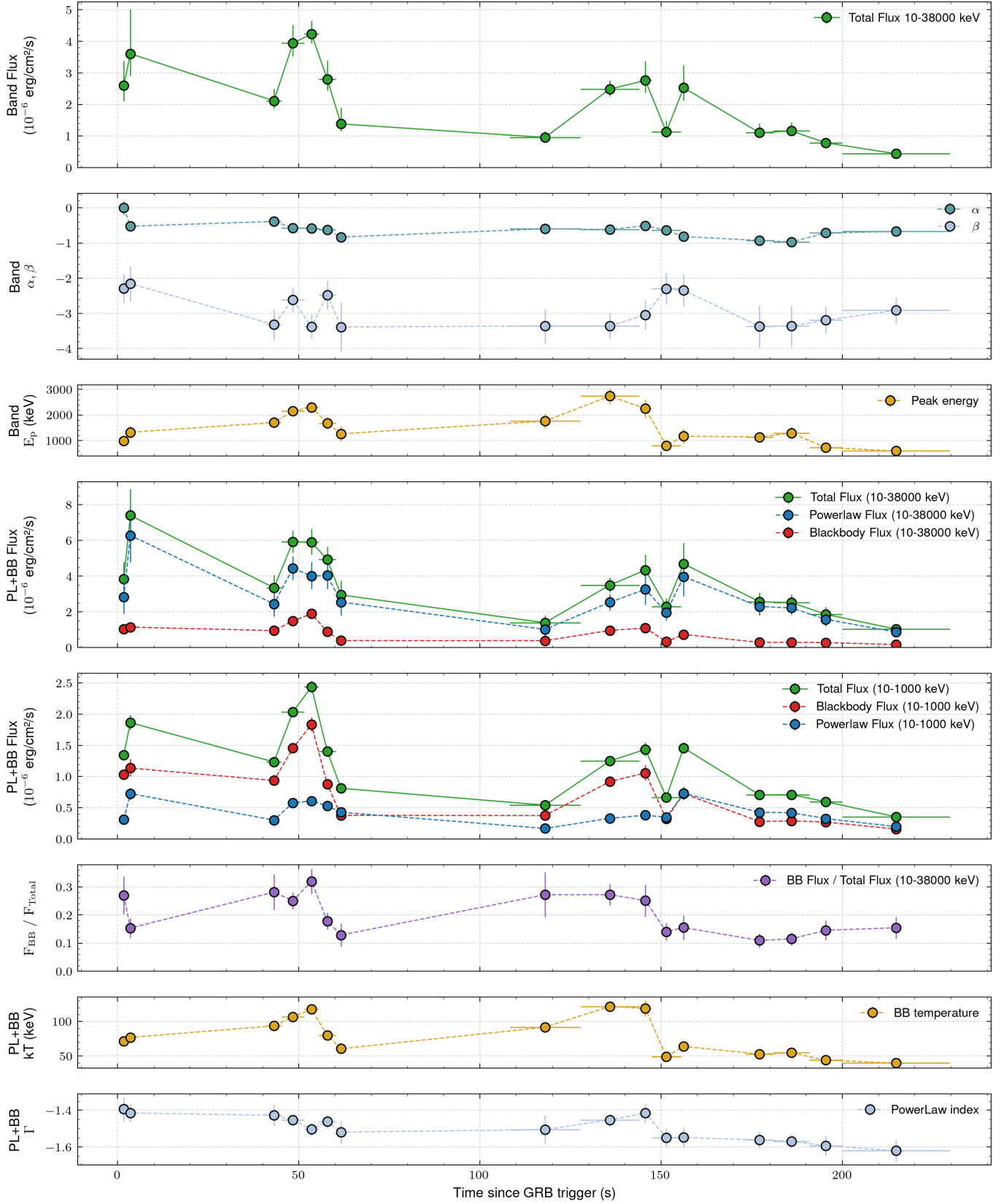


Figure 3. Time-resolved spectral evolution of GRB 230204B using both the Band and PL+BB models. Top three panels: Light curve and spectral evolution from the Band function fits in the 10–38000 keV range. The panels show (i) total flux, (ii) low- and high-energy photon indices (α , β), and (iii) peak energy (E_p). Bottom five panels: Temporal evolution from the Power-law + Blackbody (PL+BB) model. Shown are: (iv) total flux along with separate contributions from the PL and BB components in 10–38000 keV, (v) their fluxes in 10–1000 keV, (vi) the ratio of BB to total flux, (vii) blackbody temperature (kT), and (viii) the PL photon index (Γ).

Table 1. Time-averaged Spectral Fitting Parameters for time-integrated and episode-wise analysis of GRB 230204B

Function	Parameters	Time-Integrated	Episode 1	Episode 2	Episode 3	Episode 4
Time range (from T_0)	Start time (s)	−0.81	−0.81	36.16	108.22	171.65
	End time (s)	229.96	5.50	69.13	162.56	229.96
Band	$K (\times 10^{-3})$ $\text{keV}^{-1} \text{ s}^{-1} \text{ cm}^{-2}$	7.77 ± 0.36	27.6 ± 2.3	14.1 ± 0.4	9.2 ± 0.3	13.3 ± 1.1
	α	$-0.83^{+0.06}_{-0.04}$	$-0.34^{+0.09}_{-0.11}$	$-0.67^{+0.04}_{-0.04}$	$-0.79^{+0.05}_{-0.05}$	$-0.82^{+0.07}_{-0.05}$
	β	$-3.39^{+0.91}_{-0.15}$	$-2.40^{+0.13}_{-0.69}$	$-2.91^{+0.33}_{-0.31}$	$-3.38^{+0.66}_{-0.05}$	$-2.72^{+0.33}_{-0.46}$
	E_p (keV)	560^{+48}_{-63}	371^{+61}_{-30}	690^{+53}_{-44}	796^{+88}_{-86}	288^{+27}_{-29}
	AIC	7340	3473	5311	5875	5801
	BIC	7356	3462	5300	5866	5794
Cutoff Power Law	K $\text{keV}^{-1} \text{ s}^{-1} \text{ cm}^{-2}$	0.33 ± 0.06	0.13 ± 0.05	0.31 ± 0.05	0.35 ± 0.07	0.60 ± 0.13
	α	$-0.81^{+0.03}_{-0.06}$	$-0.40^{+0.10}_{-0.10}$	$-0.67^{+0.03}_{-0.04}$	$-0.79^{+0.03}_{-0.05}$	$-0.83^{+0.04}_{-0.07}$
	E_p (keV)	552^{+68}_{-36}	424^{+50}_{-22}	704^{+55}_{-37}	786^{+123}_{-56}	300^{+34}_{-17}
	AIC	7361	3484	5330	5895	5822
	BIC	7372	3496	5341	5906	5833
Power Law + Blackbody	K_{PL} $\text{keV}^{-1} \text{ s}^{-1} \text{ cm}^{-2}$	2.71 ± 0.30	2.95 ± 0.56	4.02 ± 0.35	3.46 ± 0.39	5.35 ± 0.67
	$K_{BB} (\times 10^{-6})$ $\text{keV}^{-3} \text{ s}^{-1} \text{ cm}^{-2}$	1.19 ± 0.18	3.71 ± 0.57	1.22 ± 0.13	0.67 ± 0.12	4.49 ± 0.73
	Γ_{PL}	$-1.49^{+0.03}_{-0.04}$	$-1.44^{+0.03}_{-0.05}$	$-1.46^{+0.02}_{-0.02}$	$-1.49^{+0.02}_{-0.03}$	$-1.58^{+0.02}_{-0.04}$
	kT (keV)	$65.4^{+3.2}_{-2.9}$	$64.9^{+3.2}_{-3.0}$	$87.32^{+2.8}_{-3.2}$	$90.26^{+4.8}_{-5.2}$	$45.6^{+2.3}_{-2.0}$
	AIC	7327	3468	5363	5896	5778
	BIC	7342	3483	5379	5911	5793

first three bins) indicate the presence of a BB component, with the spectrum softening through the episode due to expansion of the photosphere (B.-B. Zhang et al. 2011; F. Ryde et al. 2010). The peak energy tracks the light curve intensity, ranging from $(211 \pm 23 \text{ keV})$ to $(970 \pm 108 \text{ keV})$, with a peak in the bin-8 of episode 3. β ranges from -3.39 to -2.15 . Top three panels in Figure 3 show the evolution of the flux and spectral parameters obtained from the Band model across the bins.

For the PL+BB model, the power-law index Γ lies in the range from -1.4 to -1.7 , while the BB temperature kT ranges from $39.6 \pm 2.5 \text{ keV}$ to $121 \pm 7 \text{ keV}$. Both the peak energy and the BB temperature broadly track the intensity of the light curve and show a similar trend. We find that while the PL contributes more than half the flux in the full 10 keV – 38 MeV range, the BB component dominates in the 10 – 1000 keV range (bottom four panels in Figure 3).

While R. Gupta et al. (2024) also reports the presence of a thermal component using both Band+BB and CPL+BB models, we find that the PL+BB formulation is statistically favored across most time bins and yields better-constrained parameters, making it more suitable for probing the physical properties of the jet, as discussed in §4.2.

4. PROMPT EMISSION: INTERPRETATION

4.1. Empirical correlation of global parameters

GRBs exhibit several empirical correlations among observed properties derived from both prompt and afterglow emission phases. These correlations are often used to characterize the common behavior of the jet outflows and constrain the physical properties of their progenitors. In this section, we focus on empirical correlations involving prompt emission parameters and compare the properties of GRB 230204B with known (energetic) LGRBs by utilizing the best-fit parameters from the time-integrated Band function model (Table 1). Correlations between prompt and afterglow parameters are explored separately in §7.7.

To compare with other GRBs, it is essential to calculate physical properties in a common rest-frame energy band, typically 1 – 10^4 keV . This requires transforming the observed quantities to the source rest frame using a k -correction factor, defined as:

$$k \equiv \frac{\int_{1/(1+z)}^{10^4/(1+z)} EN(E)dE}{\int_{e_1}^{e_2} EN(E)dE}, \quad (1)$$

where $N(E)$ is the spectral model in units of counts per unit energy, E the energy, and (e_1, e_2) brackets the energy band of the detector.

The isotropic equivalent energy in the rest frame, E_{iso} , is calculated as:

$$E_{\text{iso}} = \frac{4\pi D_L^2 \cdot k \cdot S_\gamma}{1+z}, \quad (2)$$

where S_γ is the gamma-ray fluence, D_L is the luminosity distance, z is the redshift of the source, and k is the k -correction factor.

For GRB 230204B, we obtain a k -correction factor of approximately 0.97 for the observed energy range of 10 – 38000 keV . The measured fluence is $S_\gamma = (1.9 \pm 0.2) \times 10^{-4} \text{ erg cm}^{-2}$. Using a luminosity distance $D_L = 5.34 \times 10^{28} \text{ cm}$, we derive an isotropic-equivalent energy $E_{\text{iso}} = (2.2 \pm 0.4) \times 10^{54} \text{ erg}$. Similarly, from the observed peak energy $E_{p,\text{obs}} = 560 \pm 55 \text{ keV}$, we calculate the rest-frame peak energy $E_p = E_{p,\text{obs}} \times (1+z) = 1758 \pm 172 \text{ keV}$.

We utilized the catalogue from L. Lan et al. (2023) to examine this GRB in the context of the Amati relation (L. Amati et al. 2002): the correlation between the GRB isotropic equivalent bolometric energy and the rest-frame peak energy. The correlation has positive dependence (Figure 4a) typically expressed as,

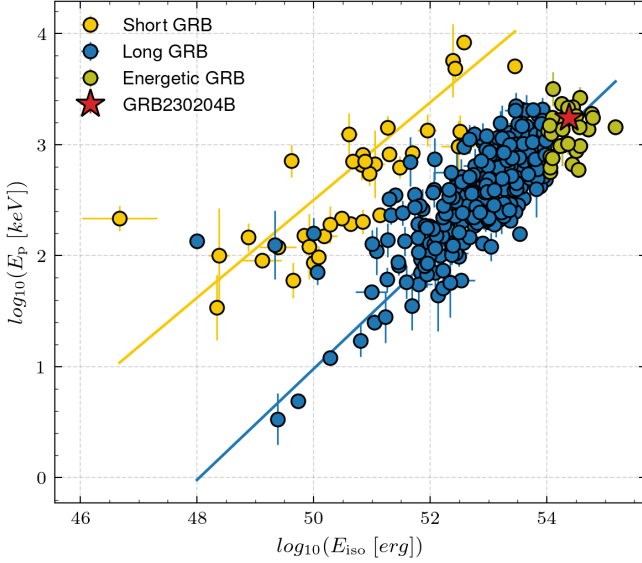
$$\frac{E_p}{100 \text{ keV}} = C \times \left[\frac{E_{\text{iso}}}{10^{52} \text{ erg}} \right]^a, \quad (3)$$

where a lies between 0.4–0.6. This relation indicates that the energetic GRBs have a tendency to release most of its energy in harder spectrum. We note that while GRB 230204B follows the relation, its E_{iso} is quite high compared to typical LGRBs, putting it in the category of highly energetic GRBs. D. Lazzati et al. (2013) proposed that GRBs dominated by photospheric emission naturally follow the Amati relation. This is in agreement with our findings for GRB 230204B, where photospheric emission plays a prominent role in the prompt phase.

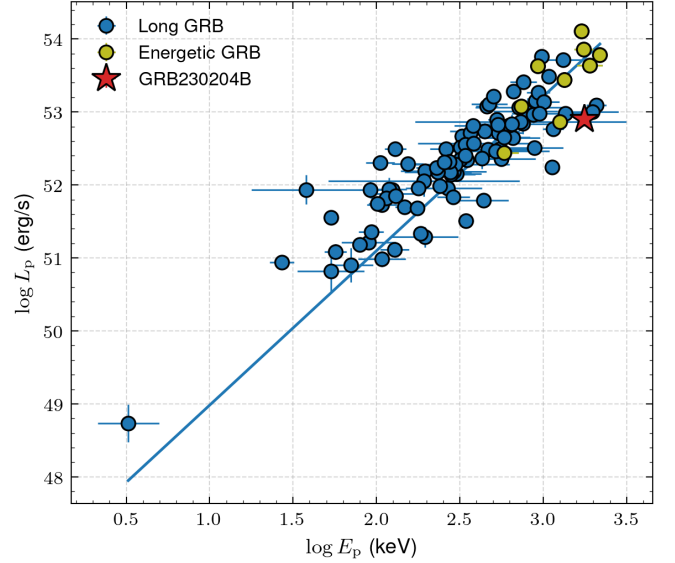
We further explored the Yonetoku relation using the catalog given in D. Yonetoku et al. (2010). It is a tighter relation (Equation 4) between the peak energy in rest frame vs peak luminosity of the GRB's prompt emission. The relation can be defined as:

$$\frac{L_p}{10^{52} \text{ erg/s}} = C \times \left[\frac{E_p}{1 \text{ keV}} \right]^b. \quad (4)$$

Our analysis gives a best-fit slope $b = 1.55 \pm 0.08$ and intercept $C = -3.52$, as illustrated in Figure 4b. The figure shows that the energetic GRBs exhibit higher values of both E_p and L_p . However, they are not clearly separated from rest of the LGRBs. For GRB 230204B, we obtain $L_p = (8.7 \pm 2.5) \times 10^{52} \text{ erg s}^{-1}$ at $T_0 + 156 \text{ s}$. This burst conforms well to the Yonetoku relation and is consistent with the population of energetic GRBs.



(a) Amati relation: Correlation between rest-frame peak energy E_p and an isotropic equivalent energy E_{iso} for GRBs with known redshifts, adapted from L. Lan et al. (2023). GRB 230204B is marked with a red star, consistent with the Amati relation and among the energetic long GRBs.



(b) Yonetoku relation: Correlation between rest-frame peak energy E_p and peak luminosity L_p , based on D. Yonetoku et al. (2010). GRB 230204B (red star) lies within the energetic GRB population and follows the correlation.

Figure 4. Correlation plots for GRB 230204B: (a) Amati relation and (b) Yonetoku relation. Both panels show that GRB 230204B belongs to the population of energetic long GRBs and conforms well to established empirical relations.

Next, we explore the Liang correlation (E.-W. Liang et al. 2010), a tight correlation between the isotropic equivalent gamma-ray energy E_{iso} and the initial bulk Lorentz factor ($\Gamma_{j,0}$) of the fireball before deceleration due to external shocks. The correlation is given by,

$$\Gamma_{j,0} \sim 182 (E_{\text{iso}}/10^{52} \text{ erg})^{(0.25 \pm 0.03)}. \quad (5)$$

Using this relation, we estimate that the bulk Lorentz factor of GRB 230204B is ~ 700 .

G. Ghirlanda et al. (2004) claimed that there exists a tight correlation between rest-frame peak energy E_p and the beaming-corrected bolometric emission energy E_γ , i.e.

$$\frac{E_p}{100 \text{ keV}} \approx 4.8 \left(\frac{E_\gamma}{10^{51} \text{ erg}} \right)^{0.7}. \quad (6)$$

Using the above relation, we find that the beaming-corrected bolometric emission energy of GRB 230204B is $\sim 6.4 \times 10^{51} \text{ erg}$, which is slightly more than the typical reservoir energy of the jet (10^{51} erg) for long GRBs.

D. A. Frail et al. (2001) found that in pre-Swift GRBs, the jet opening angle θ_0 seems to be anti-correlated with E_{iso} through $E_{\text{iso}} \propto \theta_0^{-2}$, so that the jet-corrected γ -ray energy $E_\gamma \approx (\theta_0^2/2)E_{\text{iso}}$ is roughly constant, $\approx 10^{51} \text{ erg}$ for long-duration GRBs. The implication is that long GRBs have a standard energy reservoir. Wider jets tend to have a lower energy concentration, while narrow jets have a higher energy concentration. Using this relation,

we calculated the jet opening angle as 4.4° , indicating a collimated jet — consistent with expectations for energetic GRBs (A. Panaitescu & P. Kumar 2001).

4.2. Analysis of photospheric emission

The thermal emission originates near the photospheric radius (r_{ph}), where the optical depth drops to unity and photons decouple from baryon-associated electrons. In this section, we characterize the jet outflow at the photosphere. Such an analysis requires a segment of the light curve with significant photospheric emission and a freely expanding, non-magnetized jet (F. Ryde 2004; F. Ryde & A. Pe'er 2009). At later times, the jet becomes optically thin, and the emission is typically dominated by non-thermal processes. Additionally, the curvature effect—arising from differences in photon arrival times and Lorentz boosting across a curved emitting surface—is more prominent in spectrally hard (thermal) bursts than in non-thermal ones (F. Ryde & A. Pe'er 2009). As a result, high-latitude emission can significantly contribute at late times. Thus, we exclude episodes 3 and 4 from our photospheric analysis.

The first episode of GRB 230204B, with a duration of 6.5 s, exhibits notable photospheric emission but does not have high enough signal-to-noise for time-resolved analysis. Episode 2, in contrast, is both bright and extended (lasting $\sim 34 \text{ s}$), making it an ideal candidate

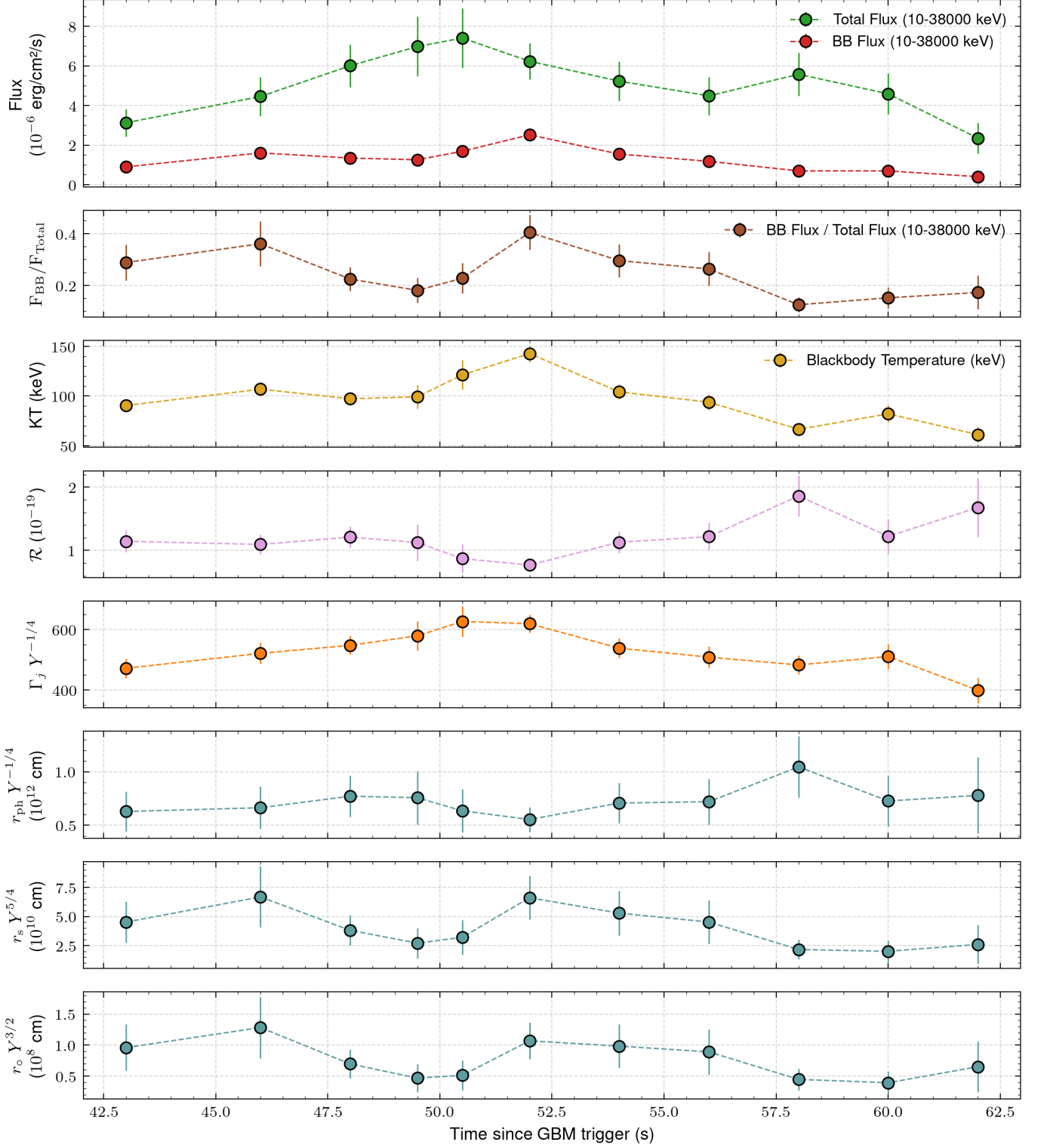


Figure 5. Time-resolved analysis of the photospheric emission during Episode 2 of GRB 230204B. From top to bottom, the panels show: (1) total flux (blue) and blackbody (BB) flux (red) in the 10-38000 keV energy range, (2) the fractional BB contribution, (3) BB temperature (kT), (4) effective transverse size of the emitting region (\mathcal{R}), (5) bulk Lorentz factor (Γ_j), (6) photospheric radius (r_{ph}), (7) saturation radius (r_s), and (8) base radius of the flow (r_0). The evolution of these parameters reflects the dynamics of the outflow at the photosphere.

for detailed photospheric modeling using finer temporal binning.

We follow the method described in A. Pe’er et al. (2007), with assumptions supported by S. Iyyani et al. (2013) and F. Ryde et al. (2010). We further divide Episode 2 into 11 smaller time bins, such that the outflow can be approximated as quasi-static within each bin. The time-resolved analysis is performed using a PL+BB function and the obtained results are available in the supplementary material at V. Swain et al. (2025)²¹. For photospheric analysis, outflow is modeled as adiabatic and follows standard fireball dynamics under the assumption of quasi-thermal emission. In each bin, we assume that a photospheric (thermal) component coexists with a non-thermal component. The evolution of the BB and total flux, their ratio and BB temperatures are shown in the upper panels of Figure 5.

Using the observed blackbody flux (F_{BB}) and temperature (T), we can define the ratio, (\mathcal{R}) as follows:

$$\mathcal{R} = \left(\frac{F_{\text{BB}}}{\sigma_{\text{SB}} T^4} \right)^{1/2}, \quad (7)$$

where σ_{SB} is the Stefan-Boltzmann constant. For GRB 230204B, \mathcal{R} ranges from $(0.76\text{--}1.86) \times 10^{-19}$: remaining nearly constant at $\sim 10^{-19}$ during the early rising phase of the light curve, and rising towards the end of the episode (Figure 5). We find that \mathcal{R} is negatively correlated with the blackbody temperature (kT) following $\mathcal{R} \propto kT^{-1.04 \pm 0.25}$ for GRB 230204B, as shown in the upper right panel of Figure 6. As a consequence, despite the effective emitting area increasing at late times, the overall blackbody flux contribution decreases due to the declining photospheric temperature.

The photospheric radius (r_{ph}) and bulk Lorentz factor (Γ_j) are two other important parameters that characterize the outflow at the photosphere. In the fireball model, the plasma expands from the base radius (r_0), accelerating until it reaches the saturation radius (r_s), beyond which the bulk Lorentz factor becomes constant, $\Gamma_j = L/\dot{M}c^2$, where L is the isotropic equivalent burst luminosity and \dot{M} is the mass ejection rate (A. Pe’er et al. 2007). The location of the photosphere (r_{ph}) relative to r_s determines whether physical parameters like Γ_j and r_{ph} can be reliably estimated. If $r_{\text{ph}} < r_s$, the flow is still accelerating with $\Gamma_j(r) \propto r$, and the relation $r_{\text{ph}}/\Gamma_j = r_0$ holds, but Γ and r_{ph} remain unconstrained.

If the blackbody flux (F_{BB}) is subdominant to the total γ -ray flux (F), i.e., $F_{\text{BB}} \ll F$, then r_{ph} will be less than r_s (A. Pe’er et al. 2007; S. Iyyani et al. 2013).

For GRB 230204B, the ratio F_{BB}/F ranges from 0.12 to 0.40 (shown in Figure 5), allowing a reliable estimation of Γ_j and r_{ph} . In such a case, the bulk Lorentz factor is given by:

$$\Gamma_j \simeq \left(\frac{(1+z)^2 D_L Y F \sigma_T}{2m_p c^3 \mathcal{R}} \right)^{1/4}, \quad (8)$$

where D_L is the luminosity distance, F is the total observed (thermal nonthermal) γ -ray flux, σ_T is the Thomson cross section, m_p is the proton mass and Y is the ratio of total fireball energy to observed gamma-ray energy, which ranges from 1 to 2. A lower value of Y indicates that the efficiency of converting the kinetic energy of the outflow into the non-thermal component is very high. Thus, for energetic GRBs, Y is expected to be 1. The photospheric radius (r_{ph}) can be estimated as

$$r_{\text{ph}} \simeq \frac{L \sigma_T}{8\pi \Gamma_j^3 m_p c^3}, \quad (9)$$

where $L = 4\pi D_L^2 Y F$ is the isotropic equivalent burst luminosity.

As seen in Figure 5, for GRB 230204B the bulk Lorentz factor ranges from 400–626 and tracks the total flux intensity. On other hand, the photospheric radius is almost constant around $(0.5 - 1.0) \times 10^{12}$ cm.

In the lower left panel of Figure 6, we show the relation between the total flux and the bulk Lorentz factor and it follows $F \propto \Gamma_j^{(2.38 \pm 0.73)}$. The correlation between the blackbody temperature and the Lorentz factor is shown in the lower right panel of Figure 6 and follows $\Gamma_j \propto T^{(0.43 \pm 0.10)}$. This suggests that the total radiated flux is sensitive to changes in the Lorentz factor, consistent with expectations from emission due to internal shocks. In the fireball models, both the temperature and bulk Lorentz factor evolve coherently during the acceleration and coasting phases of the jet. In contrast, the photospheric radius is remarkably stable compared to the variations in temperature and flux. A similar feature has been seen in the case of the thermally bright GRB 090902B (F. Ryde et al. 2010).

The radius at the base of the flow (r_0) which is independent of the cases ($r_{\text{ph}} < r_s$ and $r_{\text{ph}} > r_s$), is given by

$$r_0 \simeq \frac{D_L \mathcal{R}}{(1+z)^2} \left(\frac{F_{\text{BB}}}{Y F} \right)^{3/2}. \quad (10)$$

Finally, the saturation radius is $r_s = \Gamma_j \times r_0$, depends on Γ_j , and hence, can be defined only for the case $r_{\text{ph}} > r_s$.

For GRB 230204B, the base radius of the outflow, r_0 , ranges from $(0.4 - 1.3) \times 10^8$ cm and the saturation radius ranges from $(2.0 - 6.7) \times 10^{10}$ cm (indicating $r_s < r_{\text{ph}}$). We find that both r_0 and r_s strongly depend on the thermal contribution to the total flux. The base radius r_0 is

²¹ https://zenodo.org/records/17782846/files/Table_PL+BB-photospheric-analysis.csv?download=1

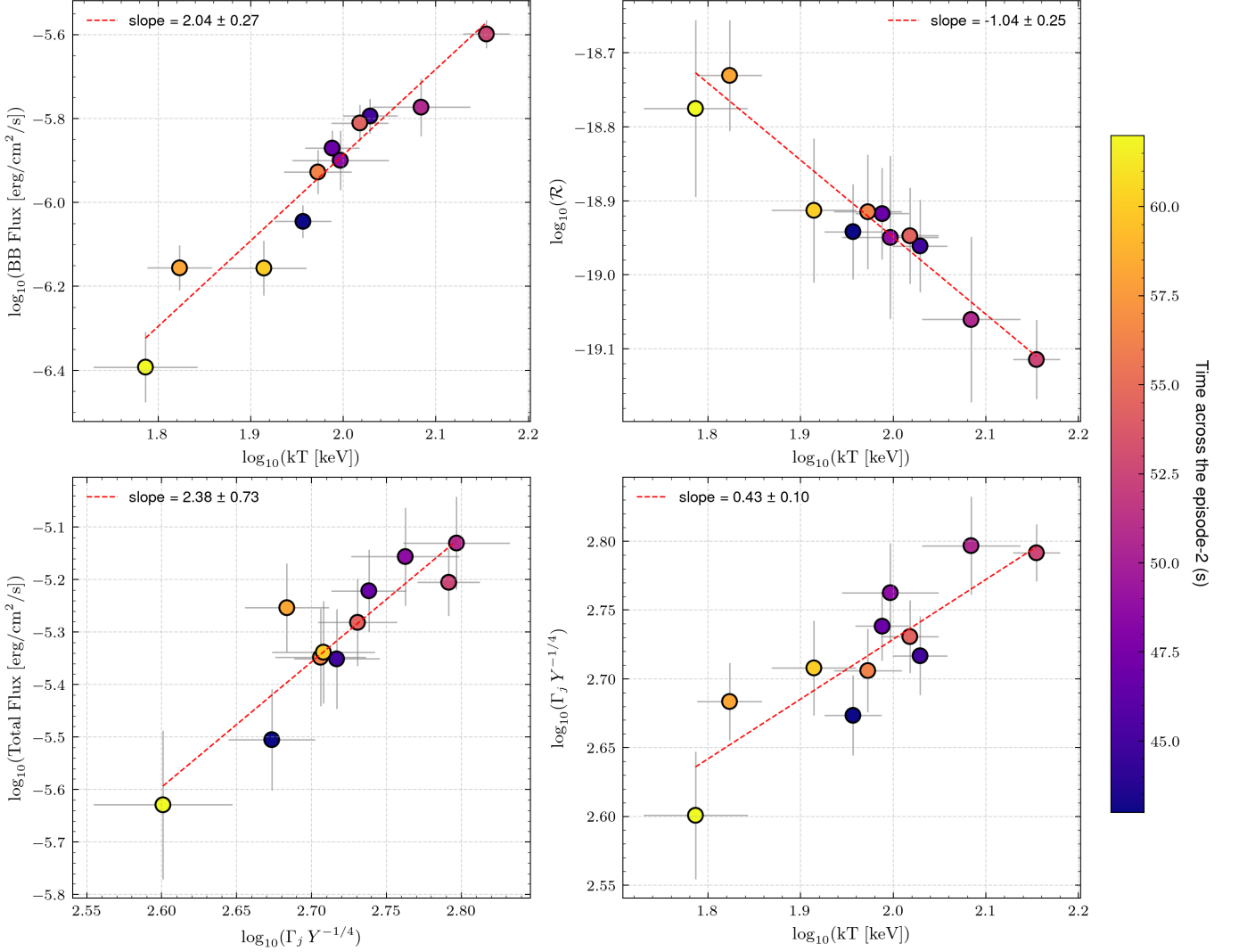


Figure 6. Correlations between photospheric parameters during Episode 2 of GRB 230204B. The upper panels display the evolution of blackbody flux and the ratio \mathcal{R} as functions of blackbody temperature. The lower-left panel shows the correlation between the total flux and the bulk Lorentz factor, while the lower-right panel presents the relation between the Lorentz factor and blackbody temperature. The color bar indicates the temporal evolution across the episode.

typically interpreted as either the Schwarzschild radius of the black hole central engine ($\sim 10^7$ cm) or the radius of the progenitor star ($\sim 10^{10}$ cm) in literature (B. Paczynski 1986). Our intermediate value of $\sim 10^8$ cm could be arising due to the significant subphotospheric emission during the acceleration phase or a moderately magnetized jet.

In summary, the time-resolved photospheric analysis of Episode 2 of GRB 230204B reveals a moderately efficient thermal component emitted within a relativistic outflow. The evolution derived from key parameters, such as the Lorentz factor, photospheric radius, and base radius, is broadly consistent with the expectations of the fireball model in the coasting phase ($r_{\text{ph}} > r_s$). The observed deviations from ideal blackbody scaling, along

with a gradual decline in thermal dominance, suggest a transition to non-thermal emission as the jet evolves. These results support a scenario in which the jet is initially weakly magnetized and launched deep within a stellar progenitor, giving rise to observable photospheric signatures as it propagates adiabatically. This detailed characterization strengthens the evidence for thermal-nonthermal interplay in the prompt emission phase of energetic long GRBs.

4.3. Origin of the non-thermal component

In this section, we discuss three possible mechanisms responsible for producing non-thermal emission in this GRB, and their connection to the thermal (photospheric) component.

In the internal shock model, internal collisions at radius $10^{17} - 10^{18}$ cm dissipate a fraction of the kinetic energy stored in the flow, producing non-thermal emission such as synchrotron radiation. For efficient internal shock emission, a significant difference in the Lorentz factors of the colliding shells is required, and the Lorentz factor of later shells should be higher (R. Hascoët et al. 2013). Since both thermal and non-thermal components are powered by the central engine, they are expected to be temporally correlated (F. Ryde et al. 2010), as we have seen in early episodes of GRB 230204B (shown in Figure 3).

A second interpretation for this correlation is that the high-energy photons could originate from Synchrotron Self-Compton (SSC) processes or Compton up-scattering of thermal photons, again leading to the power-law and blackbody components tracking each other (B.-B. Zhang et al. 2011), which we observe in GRB 230204B. Within this framework, the low-energy power-law component may arise from a different emission mechanism, such as synchrotron radiation (A. Pe’er & F. Ryde 2011). The positive slope of the power-law component in νF_ν space indicates that a substantial fraction of the energy could be emitted near or beyond the GeV range. Such high-energy photons are detectable by the *Fermi* LAT instrument, as demonstrated in cases like GRB 090902B (F. Ryde et al. 2010). However, for GRB 230204B, the LAT boresight angle was 108° , precluding the availability of LAT data to test this hypothesis.

A third possibility is that the non-thermal power-law component may arise from magnetic reconnection, where energy is transported via Poynting flux within the baryonic outflow. GRBs of this type, such as GRB 080916C, are expected to possess highly magnetized jets with purely non-thermal emission that is well-described by the Band function (A. Pe’er & F. Ryde 2011). For GRB 230204B, the presence of a blackbody component in the observed spectrum indicates that the jet is either moderately or weakly magnetized (P. Veres et al. 2012), hence this explanation is unlikely to hold true for our case. Note that in the presence of a magnetic field, the BB component could be emitted during the acceleration phase or below the saturation radius, making it impossible to determine the photospheric radius and the Lorentz factor (a case of $r_{\text{ph}} < r_s$).

5. AFTERGLOW EMISSION: ANALYSIS

We now turn our attention to the afterglow data. Afterglows are often modeled as a power-law in both spectral and temporal domains, with $F_\nu \propto t^{-\alpha} \nu^{-\beta}$, and we proceed with this analysis first. This is followed by

more sophisticated modeling in §6. All the afterglow data used in this work are available in the supplementary material at V. Swain et al. (2025)²² and plotted in Figure 7.

5.1. Temporal evolution

Within the optical band, we have the most extensive coverage in the SDSS *r* filter. These data points are well-fit by a single power-law function, giving a temporal decay rate of $\alpha = 1.82 \pm 0.01$. We do not see any rising phase, plateau, or a jet break.

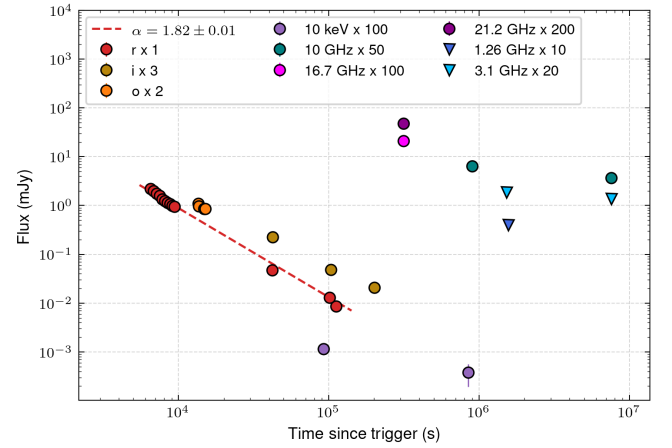


Figure 7. Multiwavelength afterglow light curves of GRB 230204B. Optical, X-ray, and radio data are shown; photometry has not been corrected for host-galaxy extinction. The *r*-band optical light curve exhibits a rapidly fading afterglow, well described by a single power-law decay.

In the *Swift*-XRT observations, we utilized two data points of unabsorbed flux density at 10 keV. These correspond to two epochs: $T_0 + (80.5\text{--}97.9)$ ks and $T_0 + (841.1\text{--}865.6)$ ks. Fitting a power-law decay to these data yields a nominal temporal decay index of $\alpha_X \approx 0.5$, which is significantly shallower than that observed in the optical band. However, the source was so faint that no centroid was determined, and some of the data could be unreliable for temporal analysis.

5.2. Spectral properties

Most of the afterglow data are not strictly simultaneous, limiting our ability to measure the spectral index β . Since we have a good fit to the *r* data, we extrapolated it to the epoch of the four o-band observations and perform a joint fit to obtain $\beta_{\text{or}} = 1.46 \pm 0.27$ in the time range from 12.7 ks to 14.3 ks. Later (at $t = 41$ ks),

²² https://zenodo.org/records/17782846/files/Table_afterglow_obs.csv?download=1

SEDM obtained consecutive data points in r and i bands, separated by just 487 s. Using these two data points, we obtain $\beta_{ri} = 2.2 \pm 0.8$ — consistent with the earlier measurement, albeit with large uncertainties.

6. AFTERGLOW MODELLING

GRB afterglow emission is dominated by synchrotron radiation, which occurs at the shock front where the ultra-relativistic outflow interacts with the circum-burst medium (CSM) surrounding the progenitor. The spectral-temporal characteristics of the afterglow depend on both the properties of the jet and those of the CSM. Thus, we can model the observations of the afterglow to constrain macrophysical parameters such as isotropic equivalent energy ($E_{K,iso}$), jet opening angle, observer viewing angle, and microphysical parameters like the power-law index of the non-thermal electrons (p), the fraction of energy in electrons (ϵ_e), the fraction of energy in magnetic field strength (ϵ_b), and the fraction of electrons and protons that are accelerated to a non-thermal distribution (χ). In this work, we take χ to be unity, indicating that all particles are being accelerated. The jet opening angle θ can be calculated if the jet break is detected, which was not the case for GRB 230204B. For a detailed analysis, we adopt a top-hat jet model, where an adiabatic blast wave describes the hydrodynamical evolution.

The temporal evolution of the afterglow shows a decaying trend in both the optical and X-ray bands, consistent with the deceleration phase of the blast wave. Since no flare is seen in the afterglow light curve, we rule out any late time energy injection.

6.1. Uniform density medium

We first consider a case of the GRB exploding in a uniform density medium. Observable parameters like α and β (§5) are expected to follow certain closure relations (H. Gao et al. 2013), and can be used to calculate properties like the electron power-law index p . Optical data show that the afterglow follows a simple power-law decay from 1.6 h to 30.8 h after the burst with $\alpha = 1.82$. These time scales correspond to the slow cooling regime, giving $p = 3.43$. This is higher than the typical range of electron power-law indices ($2 < p < 3$) expected from theoretical models of shock acceleration mechanisms (D. Miceli & L. Nava 2022) as well as from typical observations (X.-G. Wang et al. 2015). Furthermore, we note that the initial temporal decay is too rapid to be consistent with a uniform density medium, even in the absence of continued energy injection. Likewise, the nearly constant late-time radio fluxes are incompatible with the predictions for such a medium. In contrast to the model

adopted by R. Gupta et al. (2024), we therefore rule out the uniform-density scenario and proceed to model the afterglow in a wind-like circum-burst environment.

6.2. Wind-type medium

R. A. Chevalier & Z.-Y. Li (2000) extensively discusses the afterglow of a GRB exploding in a wind-type CSM. In this case, α and β depend on the relative values of the observation frequency ν , the synchrotron characteristic frequency (ν_m) and the cooling frequency (ν_c). These cases are *schematically* denoted in Figure 8 for a wind-type medium. The dashed diagonal line denotes the cooling frequency increasing with time ($\nu_c \propto t^{1/2}$), while the dotted diagonal shows the characteristic frequency decreasing with time ($\nu_m \propto t^{-3/2}$). The time (t_{cm}) when these frequencies are equal ($\nu_c = \nu_m = \nu_{cm}$) corresponds to the transition from the fast cooling to the slow cooling phase, and typically occurs at very early stages of the afterglow (R. Sari et al. 1998). Since our afterglow data starts only 1.5 hours after the burst, we can safely limit our analysis to the slow-cooling regime ($t > t_{cm}$).

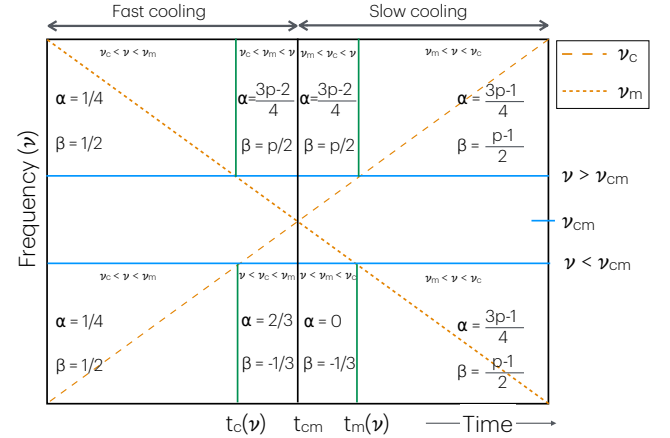


Figure 8. Schematic showing closure relations for α and β under different regimes for a wind-type medium. The frequency–time space is divided into regimes based on evolution of the synchrotron characteristic and cooling frequencies as a function of time. The relevant closure relation is identified based on the observation frequency and time. Note that the trends are indicative and the figure is not drawn to scale. Based on calculations and discussions in R. A. Chevalier & Z.-Y. Li (2000).

It is important to note that the synchrotron self-absorption frequency (ν_a) lies significantly below the optical and X-ray bands and therefore does not influence the afterglow in these bands. However, in the radio band, ν_a plays a critical role in early observations, which will be discussed later in the context of the radio afterglow.

For $t > t_{cm}$, we analyze two scenarios for the observed frequency (ν) of optical afterglow: $\nu < \nu_{cm}$ and $\nu > \nu_{cm}$. The first scenario, the flux is expected to remain constant ($\alpha = 0$) in the early stages ($t < t_m(\nu)$), where $t_m(\nu)$ is the time when the characteristic frequency passes through the observed band. Once the synchrotron characteristic frequency drops below the observational frequency, the decay steepens to $\alpha = (3p - 1)/4$. On the other hand, in the second scenario where $\nu > \nu_{cm}$, we expect the flux to decay with $\alpha = (3p - 2)/4$, followed by a slight steepening to $\alpha = (3p - 1)/4$. Note that the late-time decay index is the same in both cases.

Since the optical afterglow of GRB 230204B follows a single power-law over our observations out to 30.8 hours, we can reasonably assume that we are seeing the final stages of the afterglow. This allows us to calculate $p = 2.76 \pm 0.01$ for GRB 230204B, which aligns well with the synchrotron forward shock model. We note that this yields $\beta = 0.88$ which while being lower than our measured values of $\beta_{or} = 1.46 \pm 0.27$ and $\beta_{ri} = 2.2 \pm 0.8$, is consistent within about 2σ .

At radio frequencies, synchrotron self-absorption plays an important role, and we have to consider the relation of ν with the absorption frequency ν_a in addition to that with ν_c and ν_m discussed in Figure 8. The self-absorption frequency, ν_a , initially lies below the characteristic synchrotron frequency, ν_m , and both decrease with time. They eventually become equal at a characteristic time, denoted as t_{am} . B. Zhang et al. (2022) explored various typical scenarios in GRBs and showed that typically this occurs at very late times ($t_{am} \sim 10^3 \times t_{cm}$), beyond the timescales discussed in this work. Thus, we can proceed considering $\nu_a < \nu_m$.

This gives us three stages: (i) when $\nu < \nu_a$, self-absorption is important and the flux increases with time ($\alpha = -1$). (ii) once the absorption frequency falls below the observing frequency ($\nu_a < \nu < \nu_m$), the flux remains constant ($\alpha = 0$). (iii) Finally, when $\nu_m < \nu$, we get a power-law decay with $\alpha = (3p - 1)/4$. Note that since self-absorption is not important in stage (ii) and (iii), they are the same as the scenarios denoted in Figure 8. Constant values of radio fluxes in stage (ii) are a tell-tale signature of a wind-type medium, and indeed, this is what we see in our data (§5.1, Figure 7).

6.3. Semi-analytical solutions

Based on the various considerations in §6.2, we now fit our afterglow data to calculate the physical parameters discussed at the start of §6. We assume that the jet is an adiabatic top-hat jet with high initial Lorentz factor,

with a line of sight within the opening angle of the top-hat jet.

R. A. Chevalier & Z.-Y. Li (2000) discusses that the properties of such a jet expanding into a wind-type medium depend on five key parameters. The first parameter is the isotropic equivalent kinetic energy $E_{K,iso}$ of the jet, which gets dissipated as radiation when the jet interacts with the CSM. The next two parameters are the fractions of the total energy fraction in electrons (ϵ_e) and in magnetic field (ϵ_b). Next, we have the electron energy distribution power-law index p . Lastly, the parameter A_\star is defined from the number density of the wind-type medium evolving as $n(r) = Ar^{-2}$, where,

$$A = \frac{\dot{M}}{4\pi m_p v_w} = 3 \times 10^{35} A_\star \text{cm}^{-1}, \quad (11)$$

where \dot{M} is the mass loss rate of the progenitor and v_w is the wind velocity. If the progenitor star is a Wolf-Rayet star, the scaled parameter A_\star can be defined as,

$$A_\star = \left(\frac{\dot{M}}{10^5 M_\odot} \right) \left(\frac{v_w}{1000 \text{ km s}^{-1}} \right)^{-1}. \quad (12)$$

Given a set of parameter values, we can determine the values of ν_c , ν_m , and ν_a and thereby calculate the fluxes at various frequencies as a function of time, following J. Granot & R. Sari (2002). To find the parameter values, we perform a fit with a Nested Sampling Monte Carlo library MultiNest using PyMultiNest (J. Buchner et al. 2014) package with 2000 n-live points. The parameter range priors are listed in Table 2. The best-fit parameters and associated confidence intervals were determined by maximizing the likelihood of the model fitting the observed data. The resultant posterior is presented in Posterior-1 of Table 2.

In our initial run, we found significant degeneracies among the model parameters. The resulting posterior distributions span a wide range of values: $E_{K,iso} \in (10^{54} - 10^{57})$ erg, $\epsilon_e \in 0.03 - 0.23$, $\epsilon_b \in 10^{-6} - 10^{-4}$, and $A_\star \in 0.01 - 0.77$, all within the 95% confidence interval. However, the posterior for the electron energy index, p , is well constrained, yielding $p = 2.76 \pm 0.01$, and is consistent with the analytic estimate derived in §6.2.

To further investigate parameter degeneracies, we examine the optical and radio light curves within the context of their respective analytical regimes. Both the optical and radio afterglows lie in the slow cooling regime. The optical light curve corresponds to the decay phase with $\nu_m < \nu < \nu_c$, for which we use Equation G of Table 1 in J. Granot & R. Sari (2002) for a wind-like medium ($k = 2$). This leads to the constraint:

$$A_\star E_{K,iso,52} \epsilon_b \epsilon_e = K1, \quad (13)$$

where $K1$ is a numerical constant. For the radio light curve in the $\nu < \nu_m$ regime, we apply Equation D from Table 1 of J. Granot & R. Sari (2002) with $k = 2$ and obtain:

$$A_* E_{K,\text{iso},52}^{1/3} \epsilon_b^{1/3} \epsilon_e^{-2/3} = K2, \quad (14)$$

where $K2$ is another numerical constant. The above two equations can be reduced to,

$$A_* \epsilon_e^{-2} = K3, \quad (15)$$

$$E_{K,\text{iso},52} \epsilon_b \epsilon_e^4 = K4, \quad (16)$$

where $K3$ and $K4$ are constants.

To break the parameter degeneracy, we adopted a typical value of $\epsilon_e \sim 0.1$ (A. Panaitescu & P. Kumar 2002; S. B. Cenko et al. 2010). B. Zhang et al. (2007) set an upper limit of $\epsilon_b \lesssim 10^{-4}$ for X-ray afterglows in the regime $\nu_m < \nu_X < \nu_c$, which is likely the case for a wind-like circum-burst medium. Therefore, for subsequent analysis, we considered two values of ϵ_b : 10^{-4} and 10^{-5} .

With ϵ_e and ϵ_b fixed, the posterior samples yield $E_{K,\text{iso}} = (2.7 \pm 0.5) \times 10^{54}$ erg for $\epsilon_b = 10^{-4}$ and $E_{K,\text{iso}} = (2.7 \pm 0.5) \times 10^{55}$ erg for $\epsilon_b = 10^{-5}$. As expected from Equation 16, the product $E_{K,\text{iso}} \times \epsilon_b \sim 10^{50}$ erg remains approximately constant for a given ϵ_e . In both cases, we obtain $A_* = 0.15 \pm 0.02$ and $p = 2.76 \pm 0.01$. The value of A_* is consistent with the low-metallicity Wolf-Rayet progenitors of long GRBs (R. A. Chevalier 2003). The results are summarized in the Posterior-1 and Posterior-2 columns of Table 2.

The inferred light curve for the best-fit model corresponding to $\epsilon_e = 0.1$ and $\epsilon_b = 10^{-4}$, overlaid on the observed data, is shown in the upper panel of Figure 9. The dashed line represents the model light curve based on the median parameter values, while the shaded region indicates the 95% credible interval. The temporal evolution of the characteristic frequencies, ν_a , ν_m , and ν_c , computed from the median parameters, is shown in the lower panel. As discussed in §6.2, the characteristic frequency ν_m crosses the optical band at very early times, before our first observation, and passes through the 10 GHz band at ~ 48 days after the explosion, resulting in a slight decrease in the radio flux. The cooling frequency ν_c remains above all observational bands throughout the period of interest.

Overall, the inferred parameters and the modeled light curve provide a consistent description of the multi-wavelength afterglow evolution of GRB 230204B, supporting the interpretation of a relativistic jet expanding into a wind-type circum-burst medium. Our best-fit model is characterized by $p = 2.76 \pm 0.01$, $\epsilon_e = 0.1$, and $A_* = 0.15 \pm 0.02$, with an upper limit of $\epsilon_b \lesssim 10^{-4}$ and a lower limit of $E_{K,\text{iso}} \gtrsim 2.7 \times 10^{54}$ erg.

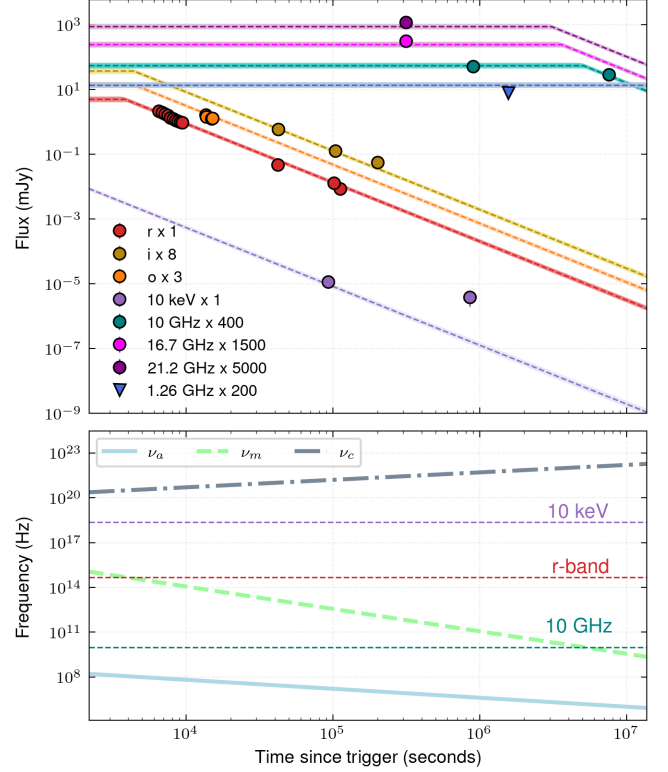


Figure 9. Afterglow modeling of GRB 230204B with an afterglow model assuming a relativistic top-hat jet propagating into a wind-type medium with the observer’s line of sight located within the jet opening angle. Upper panel shows the multi-band afterglow light curves plotted with dotted lines representing the best fit model for each band. The shaded regions indicates the 3σ uncertainty intervals from the fit. Bottom panel shows the synchrotron break frequencies ν_a , ν_m and ν_c as a function of time.

7. DISCUSSION

GRB 230204B exhibits a bright and rapid fading afterglow due to the interaction of jet with a wind-type medium. Despite its classification as an energetic GRB, based on prompt emission properties, the majority of the burst energy is converted into broadband afterglow emission. In this section, we discuss the properties of the afterglow emission and its progenitor.

7.1. Fast fading afterglow in a wind-type medium

As discussed in Section 6.2, the optical afterglow of GRB 230204B decays with a temporal index of $\alpha \sim 1.93$ in the $\nu_m < \nu < \nu_c$ regime, exhibiting a significantly steeper decline than that observed in a typical LGRB, as shown in Figure 10. In general, both a wind-like medium ($\rho \propto r^{-2}$) and a uniform interstellar medium (ISM) quickly leave the fast-cooling phase ($\nu_m > \nu_c$) and enter the slow-cooling regime ($\nu_m < \nu_c$) at very early times. In the slow-cooling case only electrons with $\gamma_e >$

Table 2. Priors and posteriors of the model parameters. The best-fit values are reported with their 95% confidence intervals.

Parameter	Unit	Prior Type	Parameter Bound	Posterior-1	Posterior-2	Posterior-3
(Fixed ϵ_e & ϵ_b)						
$\log_{10}(E_{K,\text{iso}})$	erg	uniform	[53, 58]	$55.79^{+1.96}_{-1.67}$	$54.43^{+0.07}_{-0.07}$	$55.43^{+0.07}_{-0.07}$
$\log_{10}(A_*)$	—	uniform	[-2, 0]	$-1.01^{+0.90}_{-0.78}$	$-0.83^{+0.06}_{-0.06}$	$-0.83^{+0.07}_{-0.06}$
$\log_{10}(\epsilon_e)$	—	uniform	[-2.0, -0.5]	$-1.09^{+0.45}_{-0.39}$	-1	-1
$\log_{10}(\epsilon_b)$	—	uniform	[-6, -1]	$-5.10^{+1.03}_{-0.85}$	-4	-5
p	—	uniform	[2, 3]	2.76 ± 0.01	2.76 ± 0.01	2.76 ± 0.01

γ_e (i.e. with peak emission above ν_c) cool efficiently; the bulk of the electron population, radiating near ν_m , does not cool significantly and continues to power the afterglow.

For typical parameters, the cooling frequency ν_c in the slow cooling regime lies above the optical band. The temporal evolution of ν_c differs significantly between environments: $\nu_c \propto t^{1/2}$ for the wind medium (R. A. Chevalier & Z.-Y. Li 2000) and $\nu_c \propto t^{-3/2}$ for ISM (R. Sari et al. 1998). Thus, in a wind, ν_c increases with time and stays above the optical band for the entire afterglow, while in the ISM, ν_c decreases and typically crosses the optical band at very late times ($\gtrsim 100$ days). Therefore, the optical light curve observed in most cases, including GRB 230204B, probes the adiabatic slow-cooling segment $\nu_m < \nu_{\text{opt}} < \nu_c$.

The temporal decay of the afterglow in this regime depends on the surrounding medium. In a uniform density medium, the flux decays with a power-law index $\alpha = (3p - 3)/4$, while in a wind-type medium, the decay is steeper, with $\alpha = (3p - 1)/4$. This implies that, for the same value of the electron power-law index p , the afterglow in a wind medium decays faster by $\Delta\alpha = 0.5$ in the decay slope compared to the uniform medium case. As discussed in §6.1 and §6.2, we can obtain reasonable values of p for GRB 230204B only if the medium is wind-type.

This rapid decay can be understood by examining the peak synchrotron flux $F_{\nu,\text{max}}$, which represents the maximum emissivity near the frequency ν_m in the slow-cooling regime (using the definition from R. Sari et al. 1998). In a wind-type medium, this peak flux decreases with time (scaling roughly as $t^{-1/2}$), while in a uniform density medium, it remains constant. The physical interpretation is that, in a uniform medium, the jet interacts with a constant-density environment and continuously sweeps up new material at a steady rate. In contrast, in a wind-type environment, the density decreases as r^{-2} , so the jet encounters progressively less material

as it expands, leading to less radiation dissipation, and creating a steeper decay in the afterglow flux.

7.2. Soft spectra in the afterglow

In addition to external factors such as the circumburst medium, the spectral shape of a GRB afterglow can also be influenced by intrinsic parameters of the electron population responsible for the synchrotron emission. One such key parameter is the electron energy distribution index (p) which defines the power-law behavior of shock-accelerated electrons as $N(\gamma_e) \propto \gamma_e^{-p}$, where γ_e is the Lorentz factor of electron.

For most GRB afterglows, p typically lies in the range 2.2–2.5 (R. Sari et al. 1998; A. Panaitescu & P. Kumar 2001; X.-G. Wang et al. 2015; L. Li et al. 2018). However, in the case of GRB 230204B, we find a higher value of $p \sim 2.76$, which implies a larger fraction of electrons reside at lower energies. This results in a softer spectral slope (i.e., a steeper spectral index β) in the observed afterglow emission. Physically, this means that fewer electrons exceed the cooling break γ_c , where they would lose energy rapidly, while a greater number remain near the minimum energy γ_m , where they can continue to radiate efficiently via synchrotron emission. This electron distribution thus favors extended, softer afterglow emission.

It is important to note that while the value of p determines the spectral slope and relative energy distribution among electrons, it does not affect the ordering in values of key synchrotron break frequencies ν_m , ν_c and the peak flux $F_{\nu,\text{max}}$. However, it strongly influences the shape of the synchrotron spectrum and the temporal decay of the afterglow, making it a crucial parameter in afterglow modeling.

GRB 230204B belongs to the class of highly energetic GRBs, characterized by a bright prompt emission and a luminous, rapidly fading afterglow. Such behavior is consistent with a high radiative efficiency, suggesting

that a substantial fraction of the jet energy was converted into prompt γ -rays during the explosion.

7.3. Dynamics of the relativistic outflow

The fundamental model of GRB afterglow hydrodynamics is governed by the interaction between the GRB jet and the surrounding medium (R. Sari 1997). During the very early afterglow phase, GRB ejecta dominate the dynamics, and the jet evolution is radiative in nature. Subsequently, the jet becomes adiabatic and is dominated by energy deposited in the external medium, following a self-similar solution (R. D. Blandford & C. F. McKee 1976). For the later case, the radius and Lorentz factor of the typical observed material can be obtained using the relations from R. A. Chevalier & Z.-Y. Li (2000):

$$R = 1.1 \times 10^{17} \left(\frac{1+z}{2} \right)^{-1/2} E_{52}^{1/2} A_*^{-1/2} t_{\text{days}}^{-1/4} \text{ cm}, \quad (17)$$

and

$$\gamma = 5.9 \left(\frac{1+z}{2} \right)^{-1/4} E_{52}^{1/4} A_*^{-1/4} t_{\text{days}}^{-1/4}, \quad (18)$$

where the coefficients in Equations 17 and 18 are applicable to high-frequency observations like X-ray and optical bands. For low-frequency bands like radio, the coefficients become 1.6×10^{17} and 5, respectively. The evolved bulk Lorentz factor of the jet during the self-similar decaying phase will be $\Gamma_{j, \text{BM}} = \sqrt{2}\gamma$.

For GRB 230204B, spanning from the first optical detection at $t_{\text{days}} = 0.07$ days to the final radio detection at $t_{\text{days}} = 87.4$ days, we estimate R to evolve from 1.4×10^{18} cm to 7.1×10^{19} cm, while $\Gamma_{j, \text{BM}}$ decreases from 168 to 24. Here, we adopt $E_{K, \text{iso}} = 2.7 \times 10^{54}$ erg, and the derived values can be considered lower limits. These values confirm that the jet remains relativistic throughout the observed afterglow phase and that the progenitor wind extends out to a large radius.

The initial Lorentz factor $\Gamma_{j, 0}$ represents the maximum Lorentz factor achieved during the explosion (i.e., during the coasting phase of the jet) and plays a crucial role in the fireball's composition and acceleration mechanism. For GRB 230204B, we obtained $\Gamma_{j, 0} \sim 700$ from the Liang correlation (in §4.1) and the maximum $\Gamma_j \sim 626$ is obtained after the coasting phase in the photospheric analysis (in §4.2).

7.4. Radiative efficiency

The radiative efficiency of a GRB is defined as the fraction of the total energy budget released in prompt γ -ray emission (N. M. Lloyd-Ronning & B. Zhang 2004):

$$\eta = \frac{E_{\text{iso}}}{E_{K, \text{iso}} + E_{\text{iso}}}, \quad (19)$$

where E_{iso} is the isotropic-equivalent energy emitted during the prompt phase, and $E_{K, \text{iso}}$ is the kinetic energy inferred from afterglow modeling.

For the regime $\nu_m < \nu_X < \nu_c$, $E_{K, \text{iso}}$ depends on several parameters, including ϵ_e , ϵ_b , and A_* , resulting in large uncertainties in the efficiency estimates (B. Zhang et al. 2007). For $\epsilon_b \lesssim 10^{-4}$ and $E_{K, \text{iso}} \gtrsim 2.7 \times 10^{54}$ erg, we obtain an upper limit on the radiative efficiency of $\sim 45\%$. In contrast, adopting $E_{K, \text{iso}} = 2.7 \times 10^{55}$ erg for $\epsilon_b = 10^{-5}$ yields a lower efficiency of $\sim 7.5\%$.

R. Gupta et al. (2024) inferred a large kinetic energy ($E_{K, \text{iso}} \sim 4 \times 10^{55}$ erg) and correspondingly a low radiative efficiency (4%). In contrast, our analysis suggests a broader and moderately higher efficiency range, consistent with values typically inferred for energetic GRBs. This difference highlights the sensitivity of radiative efficiency estimates to assumptions about the circum-burst environment and the adopted microphysical parameters.

7.5. Collimated outflow

While the jet remains relativistic, the observed light curve can be adequately modeled using a spherical expansion framework. However, once the jet decelerates sufficiently, edge effects become prominent due to the lateral expansion of the jet (J. E. Rhoads 1999; R. Sari & T. Piran 1999). This transition results in a significantly steeper light curve evolution during the edge expansion phase. The edge effect becomes observable when the Lorentz factor of the jet becomes comparable to the inverse of the jet's angular half-opening angle ($\Gamma_j \sim 1/\theta_0$). Following R. A. Chevalier & Z.-Y. Li (2000), the characteristic time at which edge effects become visible is:

$$t_{\text{edge}} = \left(\frac{1+z}{2} \right) \left(\frac{\theta_0}{0.2} \right)^4 E_{52} A_*^{-1} \text{ days}, \quad (20)$$

where θ_0 is the jet half-opening angle in radians, E_{52} is the isotropic-equivalent kinetic energy ($E_{K, \text{iso}}$) in units of 10^{52} erg, and A_* is the wind parameter.

Analysis of the GRB 230204B light curve reveals that up to the final radio detection at ~ 87 days, the jet remained relativistic with $\Gamma_{j, \text{BM}} \sim 24$ and no steepening was observed in the light curve. This places a lower limit on the jet opening angle of $\theta_0 > 4.8^\circ$ for $E_{K, \text{iso}} \gtrsim 2.7 \times 10^{54}$ erg and $\theta_0 > 2.7^\circ$ for $E_{K, \text{iso}} \gtrsim 2.7 \times 10^{55}$ erg. This limit is consistent with our independently derived estimate of $\theta_0 \approx 4.4^\circ$ (§4.1), obtained from the empirical correlation of D. A. Frail et al. (2001). Our constraint is consistent with the independent broadband modeling by R. Gupta et al. (2024), who also infer a narrow and highly collimated jet based on afterglow fitting assuming a top-hat geometry and an ISM circum-burst medium using `afterglowpy`.

S. B. Cenko et al. (2010) found that the highly energetic GRBs can have a true energy release of $E_{tot} \gtrsim 10^{52}$ erg. For GRB 230204B, considering the collimated jet adopting $\theta_0 \sim 5^\circ$, $E_{K,iso} \gtrsim 2.7 \times 10^{54}$ erg, and $E_{iso} \sim 2.2 \times 10^{54}$ erg, we estimate a total energy release of $E_{tot} \gtrsim 1.9 \times 10^{52}$ erg. These results place GRB 230204B among the class of hyper-energetic GRBs.

7.6. Implications of Wind Parameter for GRB Progenitor

Considering the observed wind interaction in GRB 230204B, the most plausible scenario is that the progenitor of GRB 230204B was a Wolf-Rayet (WR) star. Galactic WR stars typically exhibit wind velocities of $\sim 1000 \text{ km s}^{-1}$ and mass loss rates of $\sim 10^{-5} \text{ M}_\odot \text{ yr}^{-1}$ (S. Woosley & J. Bloom 2006). However, our derived wind parameter $A_\star \sim 0.15$ for GRB 230204B implies a lower mass loss rate of $(1.5 \pm 0.2) \times 10^{-6} \text{ M}_\odot \text{ yr}^{-1}$. Mass loss in the WR phase plays a critical role in determining the final fate of the star—excessive loss can strip the core, favoring neutron star formation and preventing the formation of the massive, rapidly rotating core needed for GRB production. Moderate mass loss rates, on the other hand, preserve sufficient core mass and angular momentum, aligning with the collapsar model (S. Woosley & J. Bloom 2006). Metallicity further influences this outcome: low-metallicity WR stars have reduced mass-loss rates and are more likely to retain the rapid rotation necessary to power a jet (A. I. MacFadyen et al. 2001; S. Woosley & J. Bloom 2006). Thus, the mass loss rate inferred for GRB 230204B is consistent with this theoretical framework, supporting a low-metallicity WR progenitor that underwent moderate mass loss while retaining sufficient core mass and angular momentum to produce a successful GRB.

7.7. Correlation Between Prompt and Afterglow Parameters

In this section, we collected two samples of GRBs to study the correlation between prompt and afterglow parameters.

For the first sample, we utilized the catalog from L. Lan et al. (2023), also used in §4.1, to obtain the redshift and prompt properties of the GRBs. To incorporate afterglow properties, we consider a collimated outflow without energy injection, i.e. $L_\nu \propto F_\nu \propto t^{-\alpha} \nu^{-\beta}$, where α and β are linearly related by closure relations depending on the medium profile and order of synchrotron frequencies (ν_a, ν_m and ν_c) (R. Sari et al. 1998; H. Gao et al. 2013).

As discussed in §7.1, most of the GRBs are observed in the adiabatic segment $\nu_m < \nu < \nu_c$, where the spectral index β is expected to be $p/2$ and α depends on the profile of the medium. From the literature, we selected a sample of 86 LGRBs that have well-sampled optical afterglow light curves covering both early and late times, ensuring that the obtained α are consistent with adiabatic segment. The derived temporal indices α for this sample are available in the supplementary material at V. Swain et al. (2025)²³.

Next, we considered a subset of 24 LGRBs from this sample for which we could reliably calculate the optical luminosity in the R or r band at 0.5 days post-burst. We used extinction-corrected data from M. G. Dainotti et al. (2024) and selected light curves with high signal-to-noise ratios. We excluded early-time data if they showed a significantly steeper decay (indicative of a reverse shock), and also excluded late-time data if they showed a change in the decay rate (indicative of jet breaks). Each light curve was then fitted with a single power-law model, $F_\nu \propto t^{-\alpha}$, to determine the temporal decay index α . The corresponding spectral indices, defined as $F_\nu \propto \nu^{-\beta}$, were compiled from various publications, which are referenced in the caption of Figure 10. For sources where R band photometry was reported instead, we converted it to r band using the β values. We then computed the k-corrected luminosity using:

$$L_\nu = F_\nu 4\pi D_L^2 (1+z)^{\beta-1}, \quad (21)$$

where D_L is the luminosity distance and F_ν is observed or calculated flux in the r band at 0.5 days.

Figure 10 presents a comparative analysis of GRB 230204B against a larger sample of LGRB. Notably, GRB 230204B exhibits a steeper decay during the adiabatic phase of the afterglow compared to most LGRBs. We find that α is correlated to isotropic equivalent energy and weakly correlated to the spectral peak energy. We also find that the r -band luminosity at 0.5 days after the burst is strongly correlated to the isotropic equivalent energy:

²³ https://zenodo.org/records/17782846/files/Table_grb-sample-correlation.csv?download=1

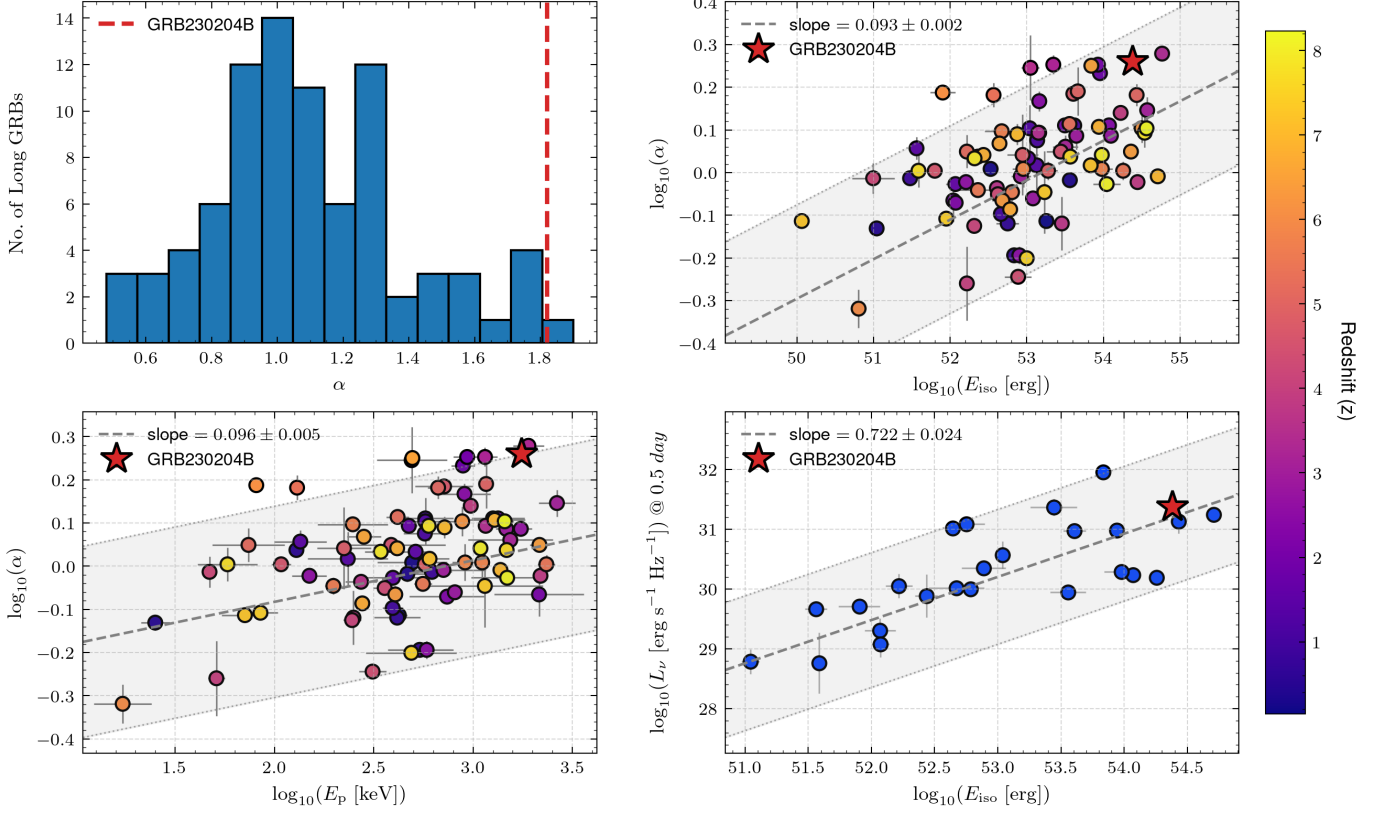


Figure 10. Top-left panel: Histogram showing the distribution of temporal power-law decay index (α) in the optical afterglow for a sample of 86 LGRBs. GRB 230204B, marked by a dashed red line, exhibits a very steep decay. Top-right panel: Correlation between α and the isotropic-equivalent prompt energy (E_{iso}), showing a positive trend (dashed line) with GRB 230204B (red star) located at the high-energy, steep-decay end. Bottom-left panel: Relation between α and the peak energy (E_p) of the prompt emission, again highlighting GRB 230204B as an outlier with high E_p and steep afterglow decay. Bottom-right panel: Afterglow optical luminosity (L_ν) at 0.5 days (rest frame, r band) as a function of E_{iso} , illustrating the correlation between prompt energy release and afterglow brightness of a sample of 24 LGRBs. The shaded region is showing the 95% confidence level of the fits. Color bar encodes GRB redshift, indicating a broad redshift distribution across the sample. The data sample is provided in the supplementary material at V. Swain et al. (2025), and the information has been compiled from multiple sources (L. Lan et al. 2023; D. A. Kann et al. 2010; B. S. Gaudi et al. 2001; S. T. Holland et al. 2007; A. M. Soderberg et al. 2006; E. Molinari et al. 2007; X.-G. Wang et al. 2015; J. Japelj et al. 2014; H. Gao et al. 2017; R. Filgas et al. 2011; M. G. Dainotti et al. 2024; T. Uehara et al. 2012; M. Nardini et al. 2014; E. S. Gorbosvsky et al. 2012; F. Olivares E. et al. 2015; B. Gendre et al. 2012; A. Cucchiara et al. 2011; M. Ackermann et al. 2013; J. Elliott et al. 2013; L.-P. Xin et al. 2016; A. N. Morgan et al. 2014; L.-Y. Huang et al. 2018; Z. Cano et al. 2014; E. Guarini et al. 2022; M. Shrestha et al. 2022; J.-S. Lian et al. 2022; P. Veres et al. 2015; K. Huang et al. 2017; L. Li et al. 2020; Y. D. Hu et al. 2019; V. M. Lipunov et al. 2016; N. Jordana-Mitjans et al. 2021; M. Marongiu et al. 2022; T. Kangas et al. 2020; Y. Tachibana et al. 2018; A. de Ugarte Postigo et al. 2018; B. Gendre et al. 2022; R. L. Becerra et al. 2019; Z.-P. Zhu et al. 2023a; L. Li & Y. Wang 2024; M. Patel et al. 2023; G. Oganessian et al. 2023; C. Angulo-Valdez et al. 2024; A. Rossi et al. 2022; Z.-P. Zhu et al. 2023b; D. Tak et al. 2025).

$$\log_{10} \alpha = (0.093 \pm 0.002) \log_{10} \left(\frac{E_{\text{iso}}}{10^{51} \text{ erg}} \right) - (4.93 \pm 0.13) \quad (22)$$

$$\log_{10} \alpha = (0.098 \pm 0.006) \log_{10} \left(\frac{E_p}{1000 \text{ keV}} \right) - (0.28 \pm 0.01) \quad (23)$$

$$\log_{10} \left(\frac{L_r}{10^{30} \text{ erg}} \right) = (0.722 \pm 0.024) \log_{10} \left(\frac{E_{\text{iso}}}{10^{51} \text{ erg}} \right) - (8.0 \pm 1.3). \quad (24)$$

These trends are broadly consistent with findings reported by S. R. Oates et al. (2015). GRB 230204B satisfies the observed correlation between the afterglow temporal decay index (α) and the isotropic-equivalent prompt energy (E_{iso}) within the 95% confidence region, as illustrated in Figure 10. Its relatively high α value is consistent with expectations for a wind-type circumburst medium, which typically produces steeper afterglow decay. In the α - E_p plane, GRB 230204B lies near the boundary of the 2- σ confidence region, indicating that the E_p is lower than expected. On the other hand,

in the L_r - E_{iso} relation, GRB 230204B clearly satisfies the correlation, owing to both the bright optical afterglow and the energetic prompt emission of this GRB.

These correlations are not predicted by the standard fireball model, which treats prompt and afterglow phases as physically decoupled, with the former arising from internal dissipation within the jet and the latter from external shocks with the circum-burst medium (R. Sari et al. 1998; P. Kumar & B. Zhang 2015). However, if both phases originate from a common energy reservoir injected by the central engine, then more energetic GRBs could naturally produce both brighter prompt emission (a few percent of the total energy) and more luminous afterglows powered by the residual kinetic energy.

Furthermore, the brightness and decay rate of the afterglow are governed by a combination of factors: (1) the density profile of the circum-burst medium, (2) the energy and internal structure of the jet, and (3) geometric effects such as the viewing angle of the observer relative to the jet axis. The first two factors strongly depend on the properties of the progenitor, and hence we may expect to see correlations in the prompt and afterglow phases of the GRB. In particular, the connection between the prompt and afterglow properties is expected to be governed by the formation of the central engine. Within the collapsar framework, the mass-loss rates and metallicity of the massive star play critical roles in the final fate of the massive star. These parameters influence whether the star can form a black hole and retain sufficient angular momentum to power a relativistic jet via an accretion disk around the central engine (S. Woosley & J. Bloom 2006). Thus, metallicity and mass-loss rates shape the jet energetics and the surrounding circum-burst medium through which the jet propagates. The third factor—the viewing angle—is an extrinsic characteristic, and may introduce scatter in these correlations.

In the forward-shock model, the brightness of the initial afterglow during the deceleration phase is primarily governed by the kinetic energy of the ejecta, the initial Lorentz factor ($\Gamma_{j,0}$) and the circum-burst medium density. More energetic GRBs interacting with denser environments are generally expected to produce brighter afterglows and exhibit an earlier onset of the decay (A. Panaitescu & W. T. Vestrand 2008). The medium profile or structure of the jet play a crucial role in determining the afterglow decay rate. Specifically, wind-type media typically result in steeper decay compared to uniform density environments, as discussed in §7.1. From our analysis, GRB 230204B is likely associated with a low metallicity Wolf-Rayet progenitor that experienced an optimal mass-loss rate to form a wind type circum-

burst medium and enough core mass to collapse into a black hole capable of driving an energetic jet. As a result, the GRB produced a highly luminous prompt emission followed by a bright optical afterglow with a steep decay slope. The properties of the prompt emission and the afterglow for GRB 230204B are broadly consistent with the correlations seen in our GRB sample. We are now exploring these correlations further with a larger data set, as a means to better understand GRBs and their progenitors.

8. SUMMARY

We presented a detailed multi-wavelength analysis of the prompt and afterglow emission of GRB 230204B, combining data from *Fermi*/GBM, *Swift*/XRT, optical facilities, and radio observatories. This GRB exhibited luminous prompt emission and had a rapidly fading bright afterglow.

The time-resolved spectral analysis of the prompt emission reveals a prominent thermal component coexisting with non-thermal radiation, providing strong evidence for photospheric emission during the early phase of the burst. Using a hybrid PL+BB model, we estimated the photospheric radius and the bulk Lorentz factor, finding a highly relativistic outflow with $\Gamma_j \sim 400 - 600$, which indicates an extreme jet powered by an efficient central engine. The unusually hard, low-energy spectral index in the initial episode ($\alpha \sim -0.34$) further supports an origin in photospheric emission. The detection of a significant blackbody component disfavors a Poynting flux-dominated jet driven by magnetic reconnection and instead suggests a baryon-loaded outflow with weak to moderate magnetization.

Using rest-frame corrections, we derive an isotropic equivalent energy of prompt emission $E_{\text{iso}} \approx 2.2 \times 10^{54}$ erg and a rest-frame peak energy $E_p \approx 1.8$ MeV, placing GRB 230204B among the group of energetic GRBs. The burst is consistent with the Amati and Yonetoku relations. Empirical correlations further revealed a significant initial Lorentz factor ($\Gamma_j \sim 700$) and a narrow jet opening angle ($\theta_0 \sim 4.4^\circ$), indicating a collimated jet.

The optical afterglow was rapidly fading, with a decay index $\alpha \sim 1.82$. Joint optical, X-ray, and radio modeling rules out a uniform-density medium, favoring a wind-type environment indicative of a massive stellar progenitor instead. In a wind medium, the temporal decay index is inherently steeper than in a uniform medium because the decreasing density causes the peak synchrotron flux to drop over time, resulting in less radiation dissipation and faster fading. The inferred wind parameter ($A_\star \sim 0.1$) points toward a low-metallicity

Wolf-Rayet progenitor. Low metallicity ensures moderate mass loss, allowing the star to retain the necessary core mass and angular momentum required by the collapsar model to power an energetic jet. The true energy $E_{tot} \gtrsim 10^{52}$ erg inferred from afterglow and prompt modeling places this GRB in the category of hyper-energetic GRBs.

GRB 230204B exhibits a positive correlation between the parameters of prompt and afterglow emission within the 95% confidence region. The standard fireball model does not predict these correlations. The burst occupies the high-energy, steep-decay end of the correlation, which is consistent with the strong interaction with the circum-burst medium expected in a wind-type medium. These observed correlations suggest that both prompt and afterglow phases originate from a common, progenitor-influenced energy reservoir, where an energetic GRB naturally produces brighter prompt emission and a luminous afterglow.

Overall, GRB 230204B represents an extreme example of a highly collimated, ultra-relativistic jet launched by a massive star in a wind environment, most likely associated with a low-metallicity Wolf-Rayet progenitor. Our results emphasize the importance of incorporating photospheric emission and wind-type circum-burst environments when modeling hyper-energetic GRBs, and support a more unified physical framework for understanding jet composition, emission mechanisms, and the true energy budget of gamma-ray bursts.

ACKNOWLEDGMENTS

We thank all the people from the GROWTH collaboration for the observation.

The GROWTH India Telescope (GIT; [H. Kumar et al. 2022](#)) is a 70-cm telescope with a 0.7-degree field of view, set up by the Indian Institute of Astrophysics (IIA) and the Indian Institute of Technology Bombay (IITB) with funding from DST-SERB and IUSSTF. It is located at the Indian Astronomical Observatory (Hanle), operated by IIA. We acknowledge funding by the IITB alumni batch of 1994, which partially sup-

ports the operations of the telescope. Telescope technical details are available at <https://sites.google.com/view/growthindia/>.

The National Radio Astronomy Observatory and Green Bank Observatory are facilities of the U.S. National Science Foundation operated under cooperative agreement by Associated Universities, Inc. We thank the staff of the GMRT that made these observations possible. GMRT is run by the National Centre for Radio Astrophysics of the Tata Institute of Fundamental Research.

Based on observations obtained with the Samuel Oschin Telescope 48-inch and the 60-inch Telescope at the Palomar Observatory as part of the Zwicky Transient Facility project. ZTF is supported by the National Science Foundation under Grant No. AST-2034437 and a collaboration including Caltech, IPAC, the Weizmann Institute of Science, the Oskar Klein Center at Stockholm University, the University of Maryland, Deutsches Elektronen-Synchrotron and Humboldt University, the TANGO Consortium of Taiwan, the University of Wisconsin at Milwaukee, Trinity College Dublin, Lawrence Livermore National Laboratories, IN2P3, University of Warwick, Ruhr University Bochum, Cornell University, and Northwestern University. Operations are conducted by COO, IPAC, and UW.

SED Machine is based upon work supported by the National Science Foundation under Grant No. 1106171

We also acknowledge the Zenodo repository for sharing our data products.

Facilities: MAXI-GSC, *Fermi*(GBM), *Astrosat*-CZTI, *Swift*(XRT), GIT:0.7m, P60/SEDm:1.5m, GMRT, VLA

Software: Astropy ([Astropy Collaboration et al. 2013, 2018, 2022](#)), Source Extractor ([E. Bertin & S. Arnouts 1996](#)), Astro-SCRAPPY ([C. McCully & M. Tewes 2019](#)), `solve-field` astrometry engine ([D. Lang et al. 2010](#)), `PSFEx` ([E. Bertin 2013](#)), ThreeML ([G. Vianello et al. 2015](#)), GDT-Fermi ([A. Goldstein et al. 2023](#))

REFERENCES

- Ackermann, M., Ajello, M., Albert, A., et al. 2012, The Astrophysical Journal Supplement Series, 203, 4, doi: [10.1088/0067-0049/203/1/4](https://doi.org/10.1088/0067-0049/203/1/4)
- Ackermann, M., Ajello, M., Asano, K., et al. 2013, ApJ, 763, 71, doi: [10.1088/0004-637X/763/2/71](https://doi.org/10.1088/0004-637X/763/2/71)
- Amati, L., Frontera, F., Tavani, M., et al. 2002, A&A, 390, 81, doi: [10.1051/0004-6361:20020722](https://doi.org/10.1051/0004-6361:20020722)
- Angulo-Valdez, C., Becerra, R. L., Pereyra, M., et al. 2024, MNRAS, 527, 8140, doi: [10.1093/mnras/stad3624](https://doi.org/10.1093/mnras/stad3624)
- Astropy Collaboration, Robitaille, T. P., Tollerud, E. J., et al. 2013, A&A, 558, A33, doi: [10.1051/0004-6361/201322068](https://doi.org/10.1051/0004-6361/201322068)
- Astropy Collaboration, Price-Whelan, A. M., Sipőcz, B. M., et al. 2018, AJ, 156, 123, doi: [10.3847/1538-3881/aabc4f](https://doi.org/10.3847/1538-3881/aabc4f)

- Astropy Collaboration, Price-Whelan, A. M., Lim, P. L., et al. 2022, *ApJ*, 935, 167, doi: [10.3847/1538-4357/ac7c74](https://doi.org/10.3847/1538-4357/ac7c74)
- Band, D., Matteson, J., Ford, L., et al. 1993, *ApJ*, 413, 281, doi: [10.1086/172995](https://doi.org/10.1086/172995)
- Becerra, R. L., Watson, A. M., Fraija, N., et al. 2019, *ApJ*, 872, 118, doi: [10.3847/1538-4357/ab0026](https://doi.org/10.3847/1538-4357/ab0026)
- Bellm, E. C., Kulkarni, S. R., Graham, M. J., et al. 2019, *PASP*, 131, 018002, doi: [10.1088/1538-3873/aaecbe](https://doi.org/10.1088/1538-3873/aaecbe)
- Bernardini, M. G., Xie, F., Sizun, P., et al. 2017, *Experimental Astronomy*, 44, 113, doi: [10.1007/s10686-017-9551-4](https://doi.org/10.1007/s10686-017-9551-4)
- Bertin, E. 2013, *Astrophysics Source Code Library*, record ascl:1301.001
- Bertin, E., & Arnouts, S. 1996, *A&AS*, 117, 393, doi: [10.1051/aas:1996164](https://doi.org/10.1051/aas:1996164)
- Bhalerao, V., Bhattacharya, D., Vibhute, A., et al. 2017, *Journal of Astrophysics and Astronomy*, 38, 31, doi: [10.1007/s12036-017-9447-8](https://doi.org/10.1007/s12036-017-9447-8)
- Blagorodnova, N., Neill, J. D., Walters, R., et al. 2018, *PASP*, 130, 035003, doi: [10.1088/1538-3873/aaa53f](https://doi.org/10.1088/1538-3873/aaa53f)
- Blandford, R. D., & McKee, C. F. 1976, *Physics of Fluids*, 19, 1130, doi: [10.1063/1.861619](https://doi.org/10.1063/1.861619)
- Buchner, J., Georgakakis, A., Nandra, K., et al. 2014, *A&A*, 564, A125, doi: [10.1051/0004-6361/201322971](https://doi.org/10.1051/0004-6361/201322971)
- Cano, Z., de Ugarte Postigo, A., Pozanenko, A., et al. 2014, *A&A*, 568, A19, doi: [10.1051/0004-6361/201423920](https://doi.org/10.1051/0004-6361/201423920)
- Casentini, C., Pittori, C., Tavani, M., et al. 2023, *GRB Coordinates Network*, 33272, 1
- Cavallo, G., & Rees, M. J. 1978, *MNRAS*, 183, 359, doi: [10.1093/mnras/183.3.359](https://doi.org/10.1093/mnras/183.3.359)
- Cenko, S. B., Frail, D. A., Harrison, F. A., et al. 2010, *The Astrophysical Journal*, 711, 641, doi: [10.1088/0004-637X/711/2/641](https://doi.org/10.1088/0004-637X/711/2/641)
- Chattopadhyay, T., Gupta, S., Iyyani, S., et al. 2022, *ApJ*, 936, 12, doi: [10.3847/1538-4357/ac82ef](https://doi.org/10.3847/1538-4357/ac82ef)
- Chevalier, R. A. 2003, *arXiv e-prints*, astro, doi: [10.48550/arXiv.astro-ph/0309637](https://doi.org/10.48550/arXiv.astro-ph/0309637)
- Chevalier, R. A., & Li, Z.-Y. 2000, *The Astrophysical Journal*, 536, 195, doi: [10.1086/308914](https://doi.org/10.1086/308914)
- Chevalier, R. A., & Li, Z.-Y. 2000, *ApJ*, 536, 195, doi: [10.1086/308914](https://doi.org/10.1086/308914)
- Coughlin, M. W., Bloom, J. S., Nir, G., et al. 2023, *The Astrophysical Journal Supplement Series*, 267, 31, doi: [10.3847/1538-4365/acdee1](https://doi.org/10.3847/1538-4365/acdee1)
- Cucchiara, A., Cenko, S. B., Bloom, J. S., et al. 2011, *ApJ*, 743, 154, doi: [10.1088/0004-637X/743/2/154](https://doi.org/10.1088/0004-637X/743/2/154)
- Dafcikova, M., Ripa, J., Pal, A., et al. 2023, *GRB Coordinates Network*, 33273, 1
- Dainotti, M. G., De Simone, B., Mohideen Malik, R. F., et al. 2024, *Monthly Notices of the Royal Astronomical Society*, 533, 4023, doi: [10.1093/mnras/stae1484](https://doi.org/10.1093/mnras/stae1484)
- de Ugarte Postigo, A., Thöne, C. C., Bolmer, J., et al. 2018, *A&A*, 620, A119, doi: [10.1051/0004-6361/201833094](https://doi.org/10.1051/0004-6361/201833094)
- Dekany, R., Smith, R. M., Riddle, R., et al. 2020, *PASP*, 132, 038001, doi: [10.1088/1538-3873/ab4ca2](https://doi.org/10.1088/1538-3873/ab4ca2)
- Elliott, J., Krühler, T., Greiner, J., et al. 2013, *A&A*, 556, A23, doi: [10.1051/0004-6361/201220968](https://doi.org/10.1051/0004-6361/201220968)
- Evans, P. A., Beardmore, A. P., Page, K. L., et al. 2007, *A&A*, 469, 379, doi: [10.1051/0004-6361:20077530](https://doi.org/10.1051/0004-6361:20077530)
- Filgas, R., Krühler, T., Greiner, J., et al. 2011, *A&A*, 526, A113, doi: [10.1051/0004-6361/201015320](https://doi.org/10.1051/0004-6361/201015320)
- Frail, D. A., Kulkarni, S. R., Sari, R., et al. 2001, *ApJL*, 562, L55, doi: [10.1086/338119](https://doi.org/10.1086/338119)
- Fremling, C., Sollerman, J., Taddia, F., et al. 2016, *A&A*, 593, A68, doi: [10.1051/0004-6361/201628275](https://doi.org/10.1051/0004-6361/201628275)
- Gao, H., Lei, W.-H., Zou, Y.-C., Wu, X.-F., & Zhang, B. 2013, *NewAR*, 57, 141, doi: [10.1016/j.newar.2013.10.001](https://doi.org/10.1016/j.newar.2013.10.001)
- Gao, H., Zhang, B., Lü, H.-J., & Li, Y. 2017, *ApJ*, 837, 50, doi: [10.3847/1538-4357/aa5be3](https://doi.org/10.3847/1538-4357/aa5be3)
- Gaudi, B. S., Granot, J., & Loeb, A. 2001, *ApJ*, 561, 178, doi: [10.1086/323244](https://doi.org/10.1086/323244)
- Gendre, B., Orange, N. B., Moore, E., et al. 2022, *ApJ*, 929, 16, doi: [10.3847/1538-4357/ac561e](https://doi.org/10.3847/1538-4357/ac561e)
- Gendre, B., Atteia, J. L., Boër, M., et al. 2012, *ApJ*, 748, 59, doi: [10.1088/0004-637X/748/1/59](https://doi.org/10.1088/0004-637X/748/1/59)
- Ghirlanda, G., Ghisellini, G., & Lazzati, D. 2004, *ApJ*, 616, 331, doi: [10.1086/424913](https://doi.org/10.1086/424913)
- Goldstein, A., Cleveland, W. H., & Kocevski, D. 2023, <https://github.com/USRA-STI/gdt-fermi>
- Gorbovskey, E. S., Lipunova, G. V., Lipunov, V. M., et al. 2012, *MNRAS*, 421, 1874, doi: [10.1111/j.1365-2966.2012.20195.x](https://doi.org/10.1111/j.1365-2966.2012.20195.x)
- Graham, M. J., Kulkarni, S. R., Bellm, E. C., et al. 2019, *PASP*, 131, 078001, doi: [10.1088/1538-3873/ab006c](https://doi.org/10.1088/1538-3873/ab006c)
- Granot, J., & Sari, R. 2002, *The Astrophysical Journal*, 568, 820–829, doi: [10.1086/338966](https://doi.org/10.1086/338966)
- Guarini, E., Tamborra, I., Bégué, D., Pitik, T., & Greiner, J. 2022, *JCAP*, 2022, 034, doi: [10.1088/1475-7516/2022/06/034](https://doi.org/10.1088/1475-7516/2022/06/034)
- Gulati, A., Leung, J., Kaplan, D., & Murphy, T. 2023, *GRB Coordinates Network*, 33321, 1
- Gupta, R., Racusin, J., Lipunov, V., et al. 2024, *arXiv e-prints*, arXiv:2412.18152, doi: [10.48550/arXiv.2412.18152](https://doi.org/10.48550/arXiv.2412.18152)
- Hascoët, R., Daigne, F., & Mochkovitch, R. 2013, *A&A*, 551, A124, doi: [10.1051/0004-6361/201220023](https://doi.org/10.1051/0004-6361/201220023)
- Holland, S. T., Boyd, P. T., Gorosabel, J., et al. 2007, *AJ*, 133, 122, doi: [10.1086/509656](https://doi.org/10.1086/509656)

- Hu, Y. D., Oates, S. R., Lipunov, V. M., et al. 2019, *A&A*, 632, A100, doi: [10.1051/0004-6361/201834959](https://doi.org/10.1051/0004-6361/201834959)
- Huang, K., Urata, Y., Takahashi, S., et al. 2017, *PASJ*, 69, 20, doi: [10.1093/pasj/psw124](https://doi.org/10.1093/pasj/psw124)
- Huang, L.-Y., Wang, X.-G., Zheng, W., et al. 2018, *ApJ*, 859, 163, doi: [10.3847/1538-4357/aaba6e](https://doi.org/10.3847/1538-4357/aaba6e)
- Iyyani, S., Ryde, F., Axelsson, M., et al. 2013, *Monthly Notices of the Royal Astronomical Society*, 433, 2739, doi: [10.1093/mnras/stt863](https://doi.org/10.1093/mnras/stt863)
- Japelj, J., Kopač, D., Kobayashi, S., et al. 2014, *ApJ*, 785, 84, doi: [10.1088/0004-637X/785/2/84](https://doi.org/10.1088/0004-637X/785/2/84)
- Jordana-Mitjans, N., Mundell, C. G., Smith, R. J., et al. 2021, *MNRAS*, 505, 2662, doi: [10.1093/mnras/stab1003](https://doi.org/10.1093/mnras/stab1003)
- Kangas, T., Fruchter, A. S., Cenko, S. B., et al. 2020, *ApJ*, 894, 43, doi: [10.3847/1538-4357/ab8799](https://doi.org/10.3847/1538-4357/ab8799)
- Kann, D. A., Klose, S., Zhang, B., et al. 2010, *ApJ*, 720, 1513, doi: [10.1088/0004-637X/720/2/1513](https://doi.org/10.1088/0004-637X/720/2/1513)
- Kasliwal, M. M., Cannella, C., Bagdasaryan, A., et al. 2019, *PASP*, 131, 038003, doi: [10.1088/1538-3873/aafbc2](https://doi.org/10.1088/1538-3873/aafbc2)
- Kumar, H., Bhalerao, V., Anupama, G. C., et al. 2022, *AJ*, 164, 90, doi: [10.3847/1538-3881/ac7bea](https://doi.org/10.3847/1538-3881/ac7bea)
- Kumar, P., & Zhang, B. 2015, *PhR*, 561, 1, doi: [10.1016/j.physrep.2014.09.008](https://doi.org/10.1016/j.physrep.2014.09.008)
- Lan, L., Gao, H., Li, A., et al. 2023, *ApJL*, 949, L4, doi: [10.3847/2041-8213/accf93](https://doi.org/10.3847/2041-8213/accf93)
- Lang, D., Hogg, D. W., Mierle, K., Blanton, M., & Roweis, S. 2010, *AJ*, 139, 1782, doi: [10.1088/0004-6256/139/5/1782](https://doi.org/10.1088/0004-6256/139/5/1782)
- Lazzati, D., Morsony, B. J., Margutti, R., & Begelman, M. C. 2013, *The Astrophysical Journal*, 765, 103, doi: [10.1088/0004-637X/765/2/103](https://doi.org/10.1088/0004-637X/765/2/103)
- Li, L., & Wang, Y. 2024, *ApJ*, 972, 195, doi: [10.3847/1538-4357/ad2511](https://doi.org/10.3847/1538-4357/ad2511)
- Li, L., Wu, X.-F., Lei, W.-H., et al. 2018, *ApJS*, 236, 26, doi: [10.3847/1538-4365/aabaf3](https://doi.org/10.3847/1538-4365/aabaf3)
- Li, L., Wang, X.-G., Zheng, W., et al. 2020, *ApJ*, 900, 176, doi: [10.3847/1538-4357/aba757](https://doi.org/10.3847/1538-4357/aba757)
- Li, Z.-Y., & Chevalier, R. A. 2003, *ApJL*, 589, L69, doi: [10.1086/376352](https://doi.org/10.1086/376352)
- Li, Z.-Y., & Chevalier, R. A. 2003, *Ambient Interaction Models for γ -Ray Burst Afterglows*, ed. K. W. Weiler (Berlin, Heidelberg: Springer Berlin Heidelberg), 419–444, doi: [10.1007/3-540-45863-8_20](https://doi.org/10.1007/3-540-45863-8_20)
- Lian, J.-S., Wang, S.-Q., Gan, W.-P., Li, J.-Y., & Liang, E.-W. 2022, *ApJ*, 931, 90, doi: [10.3847/1538-4357/ac69db](https://doi.org/10.3847/1538-4357/ac69db)
- Liang, E.-W., Yi, S.-X., Zhang, J., et al. 2010, *The Astrophysical Journal*, 725, 2209, doi: [10.1088/0004-637X/725/2/2209](https://doi.org/10.1088/0004-637X/725/2/2209)
- Lipunov, V. M., Gorosabel, J., Pruzhinskaya, M. V., et al. 2016, *MNRAS*, 455, 712, doi: [10.1093/mnras/stv2228](https://doi.org/10.1093/mnras/stv2228)
- Lloyd-Ronning, N. M., & Zhang, B. 2004, *ApJ*, 613, 477, doi: [10.1086/423026](https://doi.org/10.1086/423026)
- MacFadyen, A. I., & Woosley, S. E. 1999, *ApJ*, 524, 262, doi: [10.1086/307790](https://doi.org/10.1086/307790)
- MacFadyen, A. I., Woosley, S. E., & Heger, A. 2001, *ApJ*, 550, 410, doi: [10.1086/319698](https://doi.org/10.1086/319698)
- Marongiu, M., Guidorzi, C., Stratta, G., et al. 2022, *A&A*, 658, A11, doi: [10.1051/0004-6361/202140403](https://doi.org/10.1051/0004-6361/202140403)
- Masci, F. J., Laher, R. R., Rusholme, B., et al. 2019, *PASP*, 131, 018003, doi: [10.1088/1538-3873/aae8ac](https://doi.org/10.1088/1538-3873/aae8ac)
- Massaro, F., Grindlay, J. E., & Paggi, A. 2010, *The Astrophysical Journal Letters*, 714, L299, doi: [10.1088/2041-8205/714/2/L299](https://doi.org/10.1088/2041-8205/714/2/L299)
- McCully, C., & Tewes, M. 2019, *Astrophysics Source Code Library* <http://ascl.net/1907.032>
- Miceli, D., & Nava, L. 2022, *Galaxies*, 10, 66, doi: [10.3390/galaxies10030066](https://doi.org/10.3390/galaxies10030066)
- Molinari, E., Vergani, S. D., Malesani, D., et al. 2007, *A&A*, 469, L13, doi: [10.1051/0004-6361:20077388](https://doi.org/10.1051/0004-6361:20077388)
- Morgan, A. N., Perley, D. A., Cenko, S. B., et al. 2014, *MNRAS*, 440, 1810, doi: [10.1093/mnras/stu344](https://doi.org/10.1093/mnras/stu344)
- Nardini, M., Elliott, J., Filgas, R., et al. 2014, *A&A*, 562, A29, doi: [10.1051/0004-6361/201321525](https://doi.org/10.1051/0004-6361/201321525)
- Oates, S. R., Racusin, J. L., De Pasquale, M., et al. 2015, *MNRAS*, 453, 4121, doi: [10.1093/mnras/stv1956](https://doi.org/10.1093/mnras/stv1956)
- Oganesyan, G., Karpov, S., Salafia, O. S., et al. 2023, *Nature Astronomy*, 7, 843, doi: [10.1038/s41550-023-01972-4](https://doi.org/10.1038/s41550-023-01972-4)
- Olivares E., F., Greiner, J., Schady, P., et al. 2015, *A&A*, 577, A44, doi: [10.1051/0004-6361/201321936](https://doi.org/10.1051/0004-6361/201321936)
- Paczynski, B. 1986, *ApJL*, 308, L43, doi: [10.1086/184740](https://doi.org/10.1086/184740)
- Panaitescu, A., & Kumar, P. 2001, *ApJL*, 560, L49, doi: [10.1086/324061](https://doi.org/10.1086/324061)
- Panaitescu, A., & Kumar, P. 2002, *ApJ*, 571, 779, doi: [10.1086/340094](https://doi.org/10.1086/340094)
- Panaitescu, A., & Vestrand, W. T. 2008, *MNRAS*, 387, 497, doi: [10.1111/j.1365-2966.2008.13231.x](https://doi.org/10.1111/j.1365-2966.2008.13231.x)
- Patel, M., Gompertz, B. P., O'Brien, P. T., et al. 2023, *MNRAS*, 523, 4923, doi: [10.1093/mnras/stad1703](https://doi.org/10.1093/mnras/stad1703)
- Pe'er, A., & Ryde, F. 2011, *ApJ*, 732, 49, doi: [10.1088/0004-637X/732/1/49](https://doi.org/10.1088/0004-637X/732/1/49)
- Pe'er, A., & Ryde, F. 2024, *The Astrophysical Journal*, 976, 55, doi: [10.3847/1538-4357/ad82ed](https://doi.org/10.3847/1538-4357/ad82ed)
- Pe'er, A., Ryde, F., Wijers, R. A. M. J., Mészáros, P., & Rees, M. J. 2007, *The Astrophysical Journal*, 664, L1, doi: [10.1086/520534](https://doi.org/10.1086/520534)
- Piran, T. 2004, *Reviews of Modern Physics*, 76, 1143, doi: [10.1103/RevModPhys.76.1143](https://doi.org/10.1103/RevModPhys.76.1143)
- Poolakkil, S., Meegan, C., & Fermi GBM Team. 2023, *GRB Coordinates Network*, 33288, 1

- Poolakkil, S., Preece, R., Fletcher, C., et al. 2021, *ApJ*, 913, 60, doi: [10.3847/1538-4357/abf24d](https://doi.org/10.3847/1538-4357/abf24d)
- Rees, M. J., & Meszaros, P. 1994, *ApJL*, 430, L93, doi: [10.1086/187446](https://doi.org/10.1086/187446)
- Rhoads, J. E. 1999, *ApJ*, 525, 737, doi: [10.1086/307907](https://doi.org/10.1086/307907)
- Rigault, M., Neill, J. D., Blagorodnova, N., et al. 2019, *A&A*, 627, A115, doi: [10.1051/0004-6361/201935344](https://doi.org/10.1051/0004-6361/201935344)
- Ror, A. K., Ghosh, A., Kumar, B., et al. 2023, *GRB Coordinates Network*, 33284, 1
- Rossi, A., Frederiks, D. D., Kann, D. A., et al. 2022, *A&A*, 665, A125, doi: [10.1051/0004-6361/202243225](https://doi.org/10.1051/0004-6361/202243225)
- Ryde, F. 2004, *The Astrophysical Journal*, 614, 827–846, doi: [10.1086/423782](https://doi.org/10.1086/423782)
- Ryde, F., & Pe’er, A. 2009, *ApJ*, 702, 1211, doi: [10.1088/0004-637X/702/2/1211](https://doi.org/10.1088/0004-637X/702/2/1211)
- Ryde, F., Axelsson, M., Zhang, B. B., et al. 2010, *The Astrophysical Journal Letters*, 709, L172, doi: [10.1088/2041-8205/709/2/L172](https://doi.org/10.1088/2041-8205/709/2/L172)
- Saccardi, A., Kann, D. A., Palmerio, J., et al. 2023, *GRB Coordinates Network*, 33281, 1
- Sari, R. 1997, *arXiv e-prints, astro*, doi: [10.48550/arXiv.astro-ph/9706078](https://doi.org/10.48550/arXiv.astro-ph/9706078)
- Sari, R., & Piran, T. 1999, *The Astrophysical Journal*, 520, 641, doi: [10.1086/307508](https://doi.org/10.1086/307508)
- Sari, R., Piran, T., & Narayan, R. 1998, *ApJL*, 497, L17, doi: [10.1086/311269](https://doi.org/10.1086/311269)
- Scargle, J. D., Norris, J. P., Jackson, B., & Chiang, J. 2013, *ApJ*, 764, 167, doi: [10.1088/0004-637X/764/2/167](https://doi.org/10.1088/0004-637X/764/2/167)
- Serino, M., Iwakiri, W., Negoro, H., et al. 2023, *GRB Coordinates Network*, 33265, 1
- Shrestha, M., Steele, I. A., Kobayashi, S., et al. 2022, *MNRAS*, 516, 1584, doi: [10.1093/mnras/stac2211](https://doi.org/10.1093/mnras/stac2211)
- Smartt, S. J., Smith, K. W., Srivastav, S., et al. 2023, *GRB Coordinates Network*, 33278, 1
- Soderberg, A. M., Berger, E., Kasliwal, M., et al. 2006, *ApJ*, 650, 261, doi: [10.1086/506429](https://doi.org/10.1086/506429)
- Swain, V., Kumar, H., Waratkar, G., et al. 2023, *GRB Coordinates Network*, 33269, 1
- Swain, V., Bhalerao, V., Kumar, H., et al. 2025, *Zenodo*, doi: [10.5281/zenodo.17782846](https://doi.org/10.5281/zenodo.17782846)
- Tachibana, Y., Arimoto, M., Asano, K., et al. 2018, *PASJ*, 70, 92, doi: [10.1093/pasj/psy090](https://doi.org/10.1093/pasj/psy090)
- Tak, D., Uhm, Z. L., Paek, G. S. H., et al. 2025, *ApJ*, 978, 29, doi: [10.3847/1538-4357/ad94f4](https://doi.org/10.3847/1538-4357/ad94f4)
- Uehara, T., Toma, K., Kawabata, K. S., et al. 2012, *ApJL*, 752, L6, doi: [10.1088/2041-8205/752/1/L6](https://doi.org/10.1088/2041-8205/752/1/L6)
- van der Walt, S., Crellin-Quick, A., & Bloom, J. 2019, *The Journal of Open Source Software*, 4, 1247, doi: [10.21105/joss.01247](https://doi.org/10.21105/joss.01247)
- Veres, P., Corsi, A., Frail, D. A., Cenko, S. B., & Perley, D. A. 2015, *ApJ*, 810, 31, doi: [10.1088/0004-637X/810/1/31](https://doi.org/10.1088/0004-637X/810/1/31)
- Veres, P., Zhang, B.-B., & Mészáros, P. 2012, *The Astrophysical Journal Letters*, 761, L18, doi: [10.1088/2041-8205/761/2/L18](https://doi.org/10.1088/2041-8205/761/2/L18)
- Vianello, G., Lauer, R. J., Younk, P., et al. 2015, *arXiv e-prints*, *arXiv:1507.08343*, doi: [10.48550/arXiv.1507.08343](https://doi.org/10.48550/arXiv.1507.08343)
- Virgili, F. J., Qin, Y., Zhang, B., & Liang, E. 2012, *MNRAS*, 424, 2821, doi: [10.1111/j.1365-2966.2012.21411.x](https://doi.org/10.1111/j.1365-2966.2012.21411.x)
- Wang, X.-G., Zhang, B., Liang, E.-W., et al. 2015, *The Astrophysical Journal Supplement Series*, 219, 9, doi: [10.1088/0067-0049/219/1/9](https://doi.org/10.1088/0067-0049/219/1/9)
- Waratkar, G., Shenoy, V., Vibhute, A., et al. 2021, *GRB Coordinates Network*, 29410, 1
- Waratkar, G., Navaneeth, P. K., Shetty, P., et al. 2023, *GRB Coordinates Network*, 33268, 1
- Wijers, R. A. M. J., & Galama, T. J. 1999, *The Astrophysical Journal*, 523, 177, doi: [10.1086/307705](https://doi.org/10.1086/307705)
- Woosley, S., & Bloom, J. 2006, *Annual Review of Astronomy and Astrophysics*, 44, 507–556, doi: [10.1146/annurev.astro.43.072103.150558](https://doi.org/10.1146/annurev.astro.43.072103.150558)
- Xin, L.-P., Wang, Y.-Z., Lin, T.-T., et al. 2016, *ApJ*, 817, 152, doi: [10.3847/0004-637X/817/2/152](https://doi.org/10.3847/0004-637X/817/2/152)
- Yonetoku, D., Murakami, T., Tsutsui, R., et al. 2010, *PASJ*, 62, 1495, doi: [10.1093/pasj/62.6.1495](https://doi.org/10.1093/pasj/62.6.1495)
- Zhang, B., Liu, L.-D., Sun, T.-R., Lyu, F., & Wu, X.-F. 2022, *ApJ*, 927, 84, doi: [10.3847/1538-4357/ac4695](https://doi.org/10.3847/1538-4357/ac4695)
- Zhang, B., Liang, E., Page, K. L., et al. 2007, *The Astrophysical Journal*, 655, 989, doi: [10.1086/510110](https://doi.org/10.1086/510110)
- Zhang, B.-B., Zhang, B., Liang, E.-W., et al. 2011, *ApJ*, 730, 141, doi: [10.1088/0004-637X/730/2/141](https://doi.org/10.1088/0004-637X/730/2/141)
- Zhu, Z.-P., Xu, D., Fynbo, J. P. U., et al. 2023a, *ApJ*, 948, 30, doi: [10.3847/1538-4357/acbd96](https://doi.org/10.3847/1538-4357/acbd96)
- Zhu, Z.-P., Lei, W.-H., Malesani, D. B., et al. 2023b, *ApJ*, 959, 118, doi: [10.3847/1538-4357/ad05c8](https://doi.org/10.3847/1538-4357/ad05c8)